Stockholm University

Bachelor Thesis

Degree Project in
Earth Science 15 hp

Exploring late Pleistocene tephrochronology in the Arctic Ocean

Evelina Lindkvist

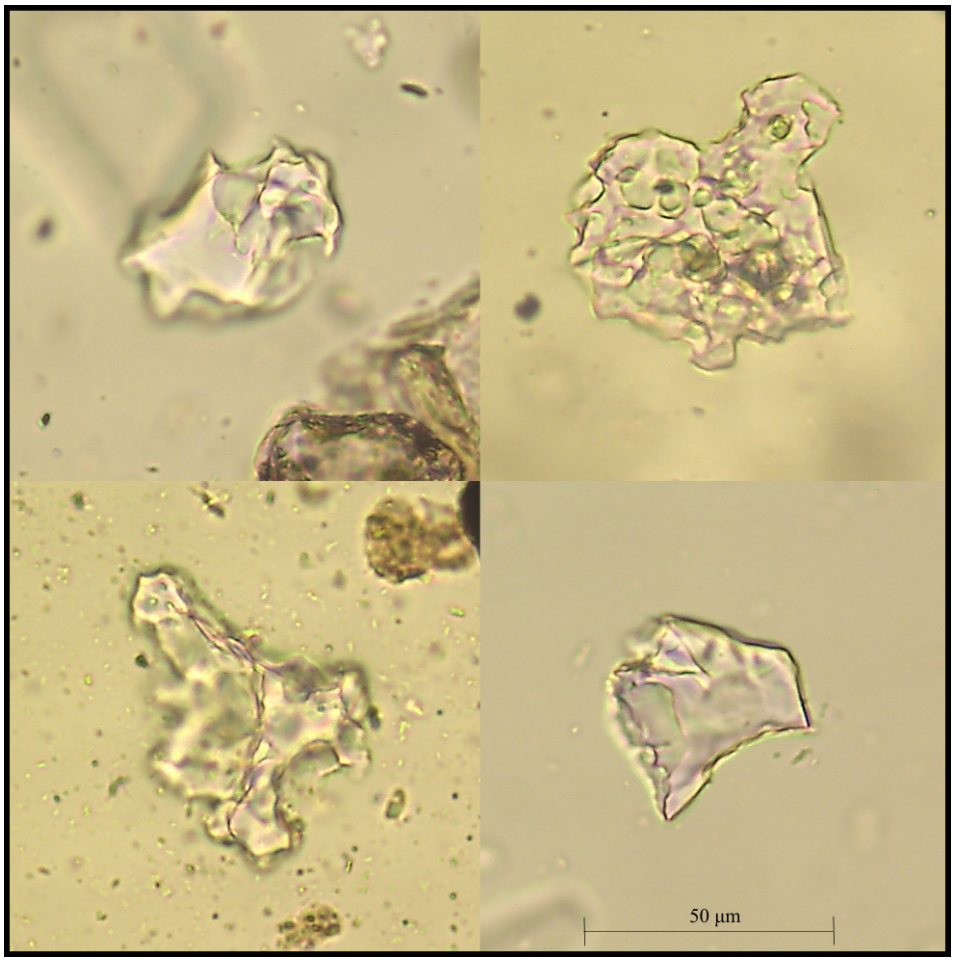

Stockholm 2024

Department of Geological Sciences
Stockholm University
SE-106 91 Stockholm

Abstract

In this study a tephra profile is obtained from sediment core SWERUS-L2-29-GC1 (between 1.06 and 4.66 mbsf) collected from the southern Lomonosov Ridge, with the purpose of analyzing whether cryptotephra horizons from late Pleistocene major volcanic eruptions have been preserved in this dynamic environment. The Old Crow and Rauchua tephras could potentially be useful isochrons in the Arctic Ocean from which absolute dates may be derived, thereby providing a critical dating-tool for the construction of robust chronological frameworks, essential for the reconstruction of paleo-environments. The tephra data is compared to two previous age-depth models derived from optically stimulated luminescence (OSL) dating; Quartz-OSL and Feldspar-OSL, in order to determine the basal age of the core. Isolation of rhyolitic shards is done via H_2O_2 treatment and SPT-density separation. A low-resolution profile of estimated shard counts is obtained where a discrete peak interval can be observed. High-resolution data collected from the peak may indicate deposition via secondary transport, and/or potential re-working of the horizon. Heterogenous shard morphologies observed throughout the studied interval are potentially related to background signals of multiple volcanic events, traced to highly explosive and silicic eruptions from the North Pacific volcanic arcs. After analyzing how the tephra signal would relate to the two different age-depth models, it's concluded that the basal age derived from the Quartz-OSL dating (early MIS 5), is more likely. Although, it's uncertain if primary ash-fall deposits of either eruptions reached the site.

Keywords: Arctic Ocean, Lomonosov Ridge, Tephrochronology, Cryptotephra

Table of Contents

1. Introduction

The Arctic region has only during the last few decades undergone alarming transitions that have manifested in e.g mass loss of glaciers and sea-ice retreat, due to the Anthropocene greenhouse-gas emissions (Shu *et al.*, 2022). Ocean-atmosphere gas exchange and the thermohaline circulation are essential modulators for the global climate, where the Arctic Ocean plays a significant role. Reconstructing paleo-environments with sediment cores - which are natural 'archives' of past climate change- is one way of studying the connection between ocean variability, climate change and associated feedback mechanisms of past environments. (Eldevik *et al.*, 2013; Bubenshchikova *et al.*, 2024). A robust geochronological framework with precise dates is needed for accurately interpreting environmental signals preserved in the marine, terrestrial and cryospheric natural archives of this region, and may be crucial for determining the rates of ongoing changes (Pearce *et al.*, 2017).

A robust chronological framework integrates several dating methods, ultimately by combining multi-proxy data of relative dating with 'absolute' dating (Larsson, 2022). The dynamic Arctic environment, with intense glacial cycles during the Quaternary Period, have led to uncertainties in many existing marine age-depth models, that often amplify in Pleistocene sediments. Relative dating methods are constrained by limited amounts of carbonate microfossils used for e.g studying biostratigraphy and conducting oxygen isotope analysis. Another dating method, based on correlating minerals magnetic polarity patterns with the placement of Earths north magnetic pole through time, is restrained by low sedimentation rates across the central Arctic Ocean and also include poorly understood reverse magnetic patterns (e.g Backman *et al.*, 2004; Faux *et al.*, 2011; Jakobsson *et al.*, 2000). 'Absolute' dates are commonly achieved with radiocarbon dating and cannot be applied to older (>45 ka) Pleistocene sediments. Additionally, large amounts of biogenetic carbon are thought to have a terrestrial origin, and uncertain reservoir ages for the Arctic water masses complicate further. (Strunk *et al.*, 2020; Backman *et al.*, 2004) A method that enables numerical ages that stretches beyond radiocarbon dates is optically stimulated luminescence dating (OSL), which can be applied to quartz or feldspar grains. This technique can determine the timing of the sediments last light exposure, and application to the unique Arctic environment have previously been successful, though some studies have reported that incomplete bleaching may yield inaccurate ages (e.g Jakobsson *et al.*, 2003; West *et al.*, 2021).

Tephrochronology is a dating method used for correlating volcanic ash deposits with known eruptions in a wide range of sediment environments (Lowe *et al.*, 2001). This could be a critical tool for improving chronologies of the Arctic marine Pleistocene sediments, though few attempts have been made. Only two studies have reported tephra results from the central Arctic Ocean basin, targeting younger Holocene eruptions (Pearce *et al.*, 2017; Ponomareva *et al.*, 2018). Recently, the Old Crow tephra horizon (~159 ka BP) was successfully identified in a new core from the Bering Sea, increasing the confidence in its age (Reyes *et al.*, 2022). A 5-cm thick ash layer of the Rauchua tephra (~177 ka BP) has also been located along the east Siberian coast (Ponomareva *et al.*, 2013). These data suggest that estimations regarding the dispersal capacity of these volcanic events need revision. This study will therefore investigate if evidence of these two eruptions have been preserved in marine core *SWERUS-L2-29-GC1* collected from the southern Lomonosov Ridge, off the East Siberian continental shelf. In this region, precise dating of marine sediments is particularly needed since bathymetric and stratigraphic data indicate that an iceshelf originated from this location, that potentially covered the entire Arctic Ocean during the Penultimate glaciation around 140 ka BP (Jakobsson *et al.*, 2016). The results will be related to two age-depth models, derived from Quartz-OSL and Feldspar-OSL dates respectively in order to evaluate what scenario the collected tephra signal suggests that the core base dates back to.

2. Background

2.1 The 'Marine Isotope Stage' framework

In the geologic history of Earth, the Quaternary Period, spanning 2.58 million years ago to present, marks the final period of the 66 million-year-long Cenozoic Era. The Quaternary is characterized by its glacial cycles and rhythmic global changes in climate and oceanography. A record of these alternating warm and cool periods is kept reflected in the oxygen isotope ratio data ($\delta^{18}O$ / $\delta^{16}O$) of shell-bearing benthic foraminifera. Expanding icesheets preferably take up the lighter ^{16}O isotope, resulting in an elevated isotopic ratio in these microfossils, preserved in the sediment record. The Marine Isotope Stages (MIS) are derived from this isotopic fractionation, and further subdivide the Quaternary timescale into longer periods of glacial cycles (even numbers), and interglacial cycles (odd numbers), see Fig. 1. (Elias, 2023) Shorter periods with colder or warmer climates within these phases are referred to as stadial- respectively interstadial substages. For example, the interglacial MIS 5 is comprised of three warmer interstadial stages (5a, 5c and 5e), and two colder stadial stages (5b and 5d). (Lisiecki *et al.*, 2005; Elias 2023) This study focus on sediments from the late Pleistocene Epoch (MIS 3-MIS 7) where glacial maxima had an approximate periodicity of 100 000 kyr, related to factors such as climate and the eccentricity of Earth's orbit (Berger *et al.*, 2010).

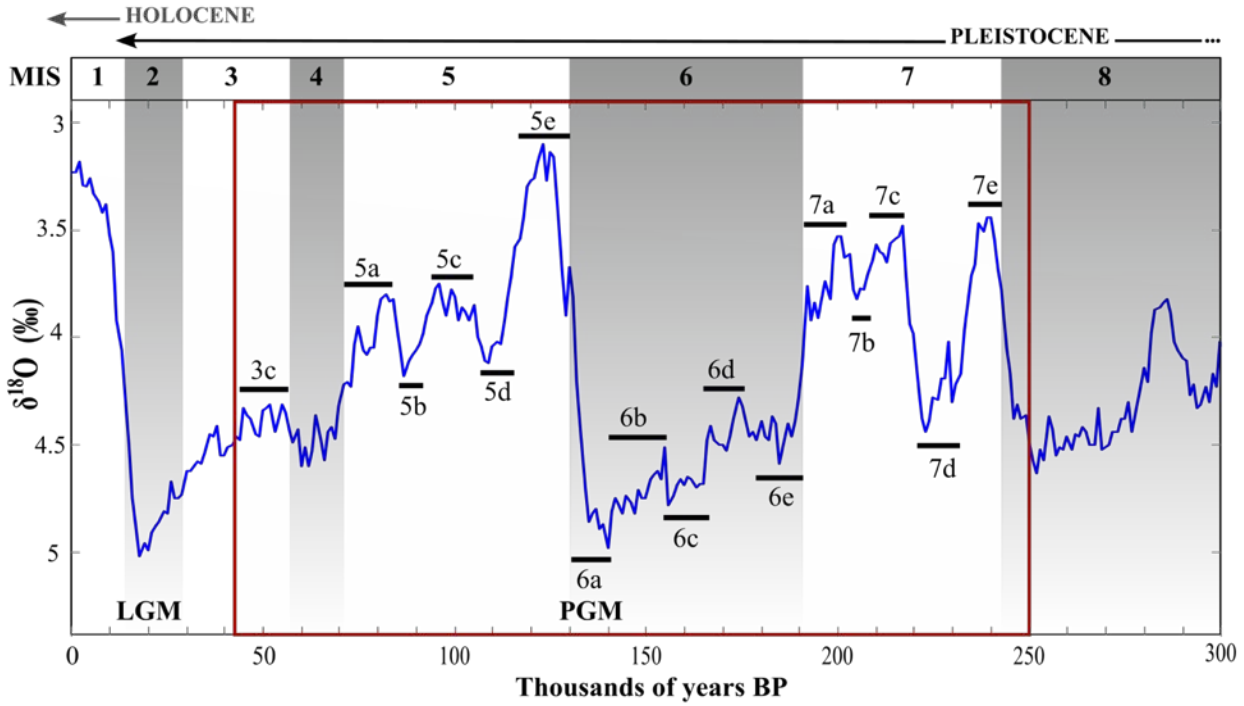

Fig. 1. MIS-stages for the last 300 kya relative to the LR_{04} global benthic stack of marine foraminiferal $\delta^{18}O$. Dataset from Lisiecki *et al.*, (2005). Arrows mark Holocene (11.7 kya - present) and Pleistocene, extending from 2.58 Mya to 11.7 kya. Time-window for this study marked in red – Late Pleistocene, with stadial and interstadial substages (Otvos, 2015; Railsback *et al.*, 2015). Abbreviations: PGM = Penultimate glacial maximum (~140 BP) and LGM = Last glacial maximum (~20 BP) the last two glacial terminations (Colleoni *et al.*, 2016).

2.2 Tephrochronology

Tephrochronology is the study of dating and correlating volcanic ash layers. Explosive volcanic eruptions can eject massive ash plumes of fine airborne fragments into the atmosphere. These unconsolidated pyroclastic products, referred to as *tephra*, can have various morphological appearances and chemical composition depending on the origin and nature of the eruption. Upon deposition, the tephra bed has provided a distinct marker in the natural archive whether it be a; lake, peat, bog, soil, glacial, or marine record, for the timing of the eruption event (if preserved). (Lowe *et al.*, 2001; Larsson, 2022) These deposits may be used as isochrons if numerical ages of the glass shards are determined, which can be done though e.g K/Ar or U-series fission track dating. Numerical dates can also be achieved by corelating the shard geochemistry, i.e the *fingerprint*, with previously dated and classified eruptions, thereby providing unique tie-points between different age models. Electron probe micro-analysis (EPMA) is widely used for attaining the composition of major oxides, and methods for establishing trace element and rare-earth element data are commonly applied as well. (Lowe, 2011)

2.3 Cryptotephra

New opportunities for the Quaternary stratigraphic and paleoenvironmental research fields were unveiled when Dugmore (1989) discovered that "invisible" tephra deposits, today known as *cryptotephras*, could be separated from their host-material and optically identified under a microscope. Only very explosive, large magnitude eruptions e.g Plinian or caldera forming eruptions (silica-rich magmas with high volatile content), are thought to generate large enough tephra volumes necessary for deposition of discrete cryptotephra markers in distal areas. (Lowe *et al.*, 2001). These very fine shards are the last ones to settle from the ash plume, and Holocene deposits from the North Atlantic Arcs have previously been located in Greenland ice-cores > 8000 km from the source vent (e.g Pearce *et al.*, 2004). To accurately determine the isochron depth, it's important to evaluate processes that may have influenced the stratigraphic position. These processes can vary depending on the specific depositional environment in question (Lowe, 2011).

2.4 Atmospheric Transport and Marine Deposition

The eruption mode is crucial for the vertical distribution of shards (Fig. 2). The direction of deposition for low eruption columns is more dependent on the prevailing tropospheric winds, which are temporary and inconsistent. Higher columns however, may reach the polar jet stream – a meandering river belt of extreme winds beneath the tropopause- and result in cryptotephra deposits in ultra-distal environments (e.g Thordarson *et al.*, 2003). Large magnitude eruptions (M > 6.5) are therefore less affected by tropospheric winds, and will (if tephra volume allows), have a broad circular distribution. (Freundt *et al.*, 2023) The plume undergoes a size fractionation through the atmospheric transportation, and beyond 300 km from the source vent mainly fine ash-sized (< 63 μm) glass shards remain (Cashman *et al.*, 2020). Air settling is considered a relative fast process (hours-days), whereas the more complex (primary) ocean settling may take years (Lowe, 2011).

Sea-ice entrainment can additionally delay the oceanic deposition with year to decades, these secondary deposits are identified in tephra layers with relative homogeneous geochemical signatures, combined with IRD and coarser lithics. Glacial or Iceberg deposition may further delay deposition with several millennia, and can potentially accumulate tephra's from other eruptions, resulting in heterogeneous signatures in a poorly-sorted grain matrix. (Freundt *et al.*, 2023)

When the shards eventually reach the ocean surface, the shift in density and viscosity slows them down significantly. Spatial displacement in the water column is also size dependent and can take place e.g in the Ekman layer (0-100 m) influenced by wind-driven currents, or across depths of neutral densities. Otherwise,

shards transport through the water column mainly controlled by gravity, although sinking ash-plumes and shard entrainment in marine snow may cross density boundaries at higher rates. (Griggs *et al.*, 2014)

On the seafloor, the shards settle out of suspension and preservation of the horizon will be favored by high sedimentation rates. Isochronous deposits ideally display homogenous signatures and a high discrete shard concentration peak. Although, different post-depositional re-working processes can dilute the horizon. (Abbott *et al.*, 2018a) Intensified bottom currents during interstadials and storm events may disperse the horizon, and lead to a gradational upward tail (from the initial peak) in the concentration profile. Another process which can lead to both upward and downwards tail-offs of low concentration intervals, is bioturbation. Finally, displacement due to sediment loading via e.g turbidity currents may also effect the isochrons credibility. (Griggs *et al.*, 2014)

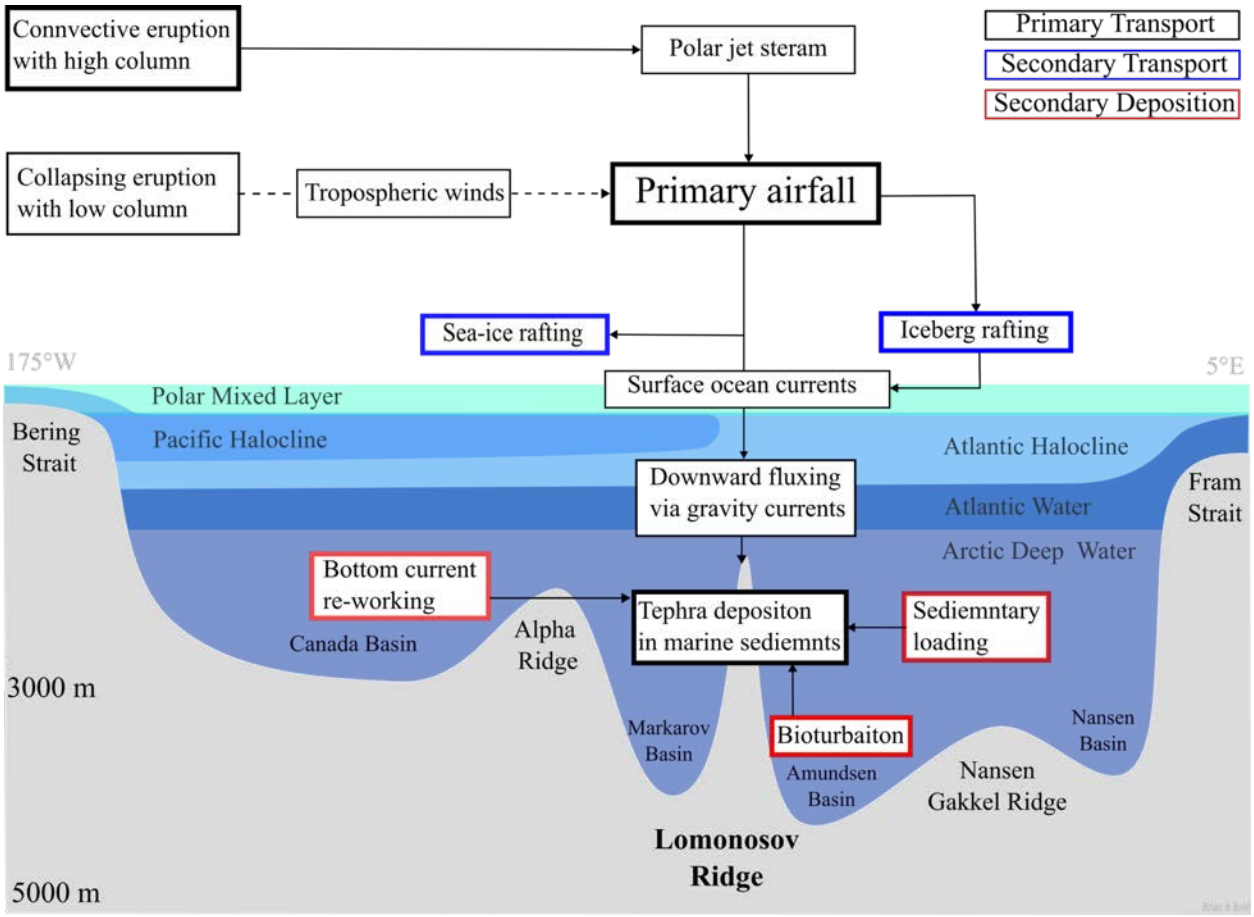

Fig. 2. Schematic illustration of the main controls influencing cryptotephra transport through the atmosphere and deposition in the Arctic Ocean. Viewed in a cross-section showing the density-stratified water masses in the Arctic Ocean. Modified from Griggs *et al.*, (2014) and Khare *et al.*, (2021).

2.5 Tracing Arctic Marine Cryptotephra

Background signals of reworked shards is an expected phenomenon in the Arctic Ocean, mainly due to the strong presence of sea-ice and iceberg rafted materials which may contribute to a continuous volcanoclastic sedimentation (Pearce *et al.*, 2017; Ponomareva *et al.*, 2018). Primary ashfall deposits are however thought to prevail over this background signal, even though isochron depths may appear to span longer intervals (Lowe, 2011). In comparison to terrestrial environments, many marine records show better spatial resolution sediments of closely related or sporadic eruptions. These are usually distinguished from one another by comparing trace- and rare earth elemental content of the glass shards, especially useful when deposits may originate from the same volcanic source. (Abbott *et al.*, 2018a) If shard morphologies display homogeneous characteristics within peaks and not between, this may also be indicative of a undisturbed horizon (e.g Katoh *et al.*, 2000).

2.6 Shard micro-morphologies

The eruption dynamics are reflected in the shard morphology and may yield information regarding processes such as magmatic fragmentation, transport and deposition. Magmatic eruptions derived from high viscosity magmas generally form clear, angular, vesicular or bubble-wall shards, often of a rhyolitic composition. If the magma has a very high content of exsolved volatiles, *pumiceous* shards may form (Fig. 3). (Bablon *et al.*, 2022). Mafic compositions are often related to brownish, blocky and larger shards, since a lower volatile content will cause a lower degree of fragmentation. (Katoh *et al.*, 2000)

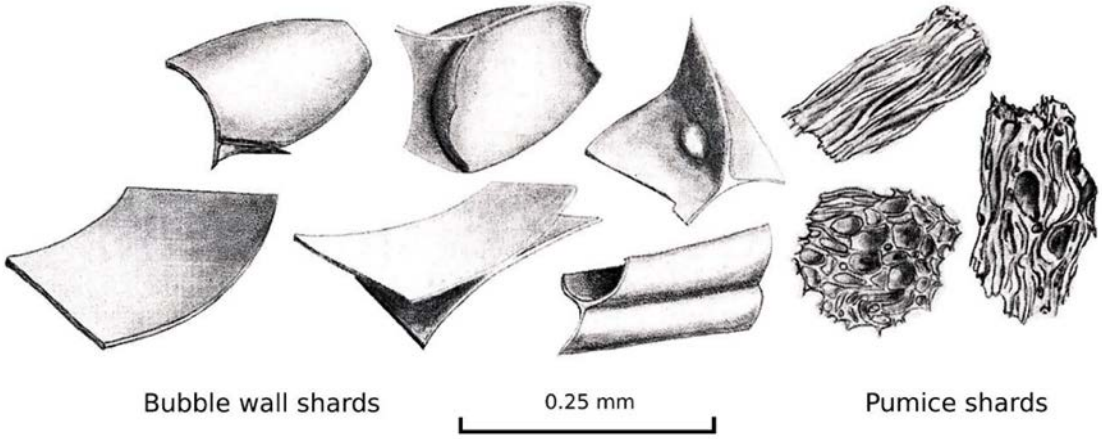

Fig. 3. Illustration of different shard morphologies**,** from Carlson, (2018). Left: Platy and blocky bubble-wall shards. Center: y-shaped bubble-wall fragments, i.e cuspate shaped. Right: Pumiceous shards (highly vesicular).

2.7 The North Pacific Arcs

The Alaska-Aleutian and Kurile-Kamchatka Arcs are known for their explosive silicic eruptions during the Quaternary. Volcanism in these regions in an effect of the North Pacific plates subduction; beneath the North American plate in the northeast - along the Aleutian trench, and under the Okhotsk microplate in the northwest, along the Kurile-Kamchatkan trench. (Lu *et al.*, 2014)

2.7.1 Alaska-Aleutian Arc – Old Crow Tephra

The Aleutian Arc is a chain of stratovolcanoes and calderas that extends from the Alaskan mainland across the Bearing Sea, towards the Kamchatka Peninsula. The most extensive Pleistocene (and Holocene) eruption from this active volcanic region is thought to have originated from a single cataclysmic eruption during middle MIS 6. The Old Crow tephra, discovered in 1983, originates from an unknown source caldera on the Aleutian arc, possibly associated with the Emmons Lake Caldera (Fig. 4, Table 1). Dating the Old Crow event has therefore been a challenge. (Westgate *et al.*, 1983; Preece *et al.*, 2011). Recently, a study from the Bering Sea identified an isochron depth for the Old Crow tephra in Core *U1345*. Since there were no signs of bioturbation and a distinct concentration peak was observed before the previous determined eruption age (~ 124 ka), its age was derived to ~159 ka. A background signal of Old Crow shards extending all the way to early MIS 5 was also observed. (Reyes *et al.*, 2022) These data indicate that the initial calculated tephra bulk volume of 200 km^3, and dispersal area constrained to Alaska and Yukon terrestrial sites need reevaluation. Background concentrations of Old Crow shards were also identified in Holocene sediments (Core *HLY0501-1*), collected from the Chukchi Sea (Ponomareva *et al.*, 2018). The Old Crow tephra has a rhyolitic composition, and shard morphologies are described as thin, platy and clear, with bubble wall fragments and junctions (Westgate *et al.*, 1983; Begét *et al.*, 1991).

2.7.2 Kurile – Kamchatkan Arc - Rauchua Tephra

This arc stretches from Hokkaido (the northernmost island of Japan), to the Kamchatka Peninsula, east of Russia. The Raucha tephra was first discovered as an outcrop on the East Siberian Sea coast (Kotov, 1998), four additional coring sites have today confirmed a dispersal area >1,500,000 km^2. Geochemical fingerprints indicate that the source vent may be located in the Karymsky volcanic center (Fig. 4, Table 2), though it hasn't been identified. In two marine cores from the Bering Sea (*SO201-2-81* and *SO201-2-40*) visible layers have been observed. A robust age-model on a lacustrine core (*ICDP Site 5011-1*) from Lake El'gygytgyn dates the event to ~177 ka (Nowaczyk *et al.*, 2013), thereby making this tephra one of the best markers for middle Pleistocene sediments in this region. The complexity of this volcanic eruption is however still poorly understood, evidence suggests a magnitude > 6.5, with a minimum bulk density tephra volume of ~ 50 km^3. Visible layers have been observed all the way to the East Russian Arctic, where a 5 cm average thick ash layer have been observed along the coast. The Rauchua tephra has a rhyolitic composition, and shards are characterized by clear, bubble-wall and fluidal textures. (Ponomareva *et al.*, 2013; Derkachev *et al.*, 2020)

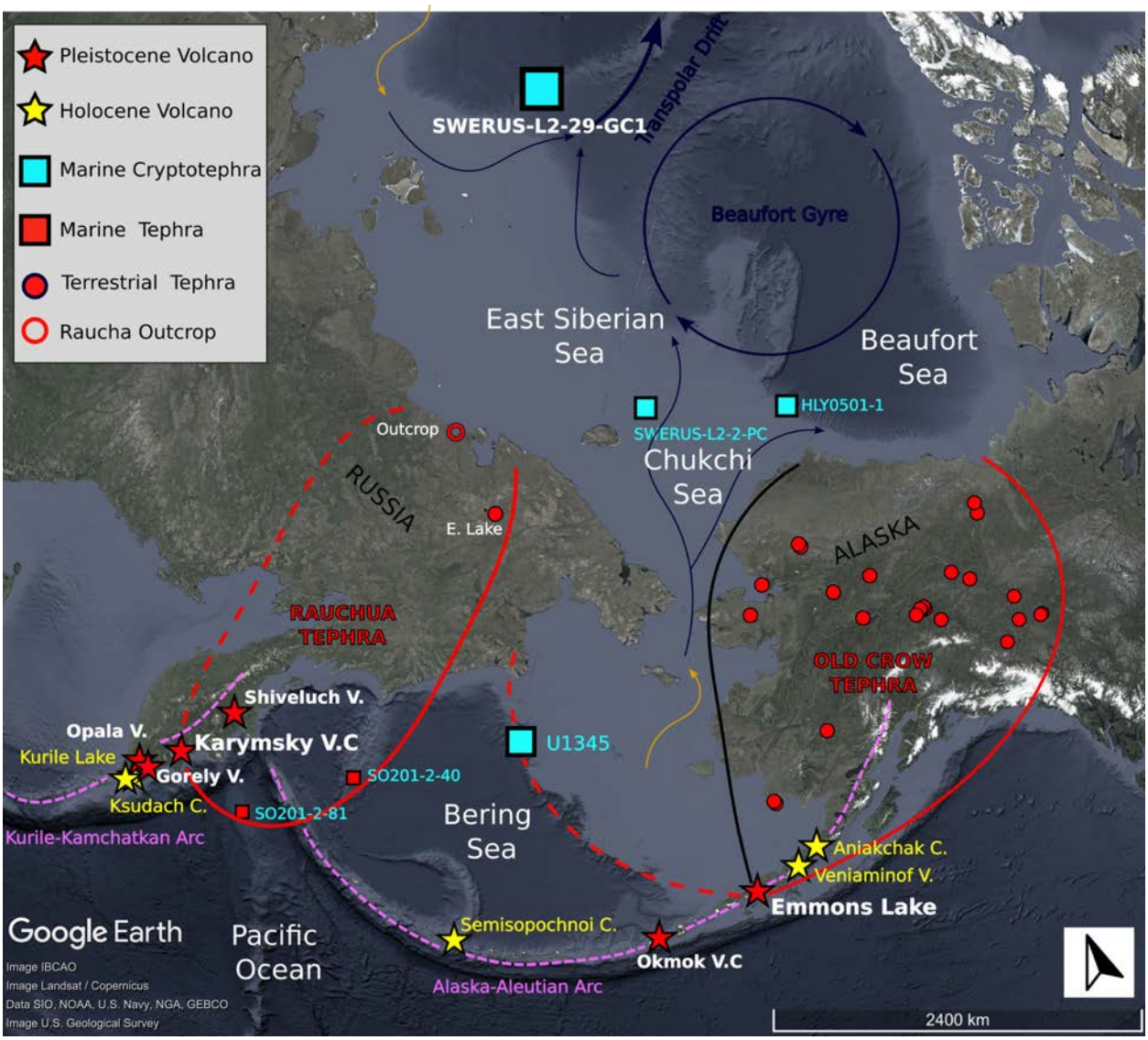

Fig. 4. Map over the Northern Pacific Ocean and Arctic Ocean showing the two major Pleistocene eruptions, dispersal areas and this reports core - *SWERUS-L2-29-GC1*. Other marine cores mentioned in the text from (Ponomareva *et al.*, 2013, 2018; Pearce *et al.*, 2017; Derkachev *et al.*, 2020; Reyes *et al.*, 2022). Emmons Lake Caldera - Old Crow tephra ~159 ka, with dispersal area from Preece *et al.*, (2011) with added data from Reyes *et al.*, (2022). Karymsky Volcanic Centre - Rauchua Tephra ~177 ka, with dispersal area from Ponomareva *et al.*, (2013). Purple marking shows the Alaska-Aleutian Arc and Kurile-Kamchatka Arc. Orange and blue arrows show major water circulation features of the Arctic Ocean (Timmermans *et al.*, 2023). Abbreviations; V = Volcano, VC = Volcanic Center, C = Caldera.
E. Lake = Lake El'gygytgyn (ICDP Site 5011-1) (Nowaczyk *et al.*, 2013).
*See Table 1 and 2 for eruption chronology.

Table 1

Major and Moderate sized eruptions from the Alaska-Aleutian Arc, and their tephra names. Pleistocene Eruptions marked with (*). Dates; Aniakchak ll (Graham *et al.*, 2016), Black Peak (Miller *et al.*, 2002), SR2 and SR4 (Derkachev *et al.*, 2020), Dawson (Davies *et al.*, 2016) and Old Crow (Reyes *et al.*, 2022).

Volcanic source	Tephra ID	Eruptions
Aniakchak Caldera	Aniakchak ll	~ 3.6 ka
Veniaminfof Volcano	Black Peak	~ 3.7 ka
Semisopochnoi Caldera	SR2	~ 12 ka
*Okmok Volcanic Centre	SR4	~ 64 ka
*Emmons Lake Caldera	Dawson and Old Crow	~ 30 resp. ~ 159 ka

Table 2

Major and Moderate Eruptions from Kurile-Kamchatkan Arc, and their tephra names. Pleistocene Eruptions marked with (*). Dates; KS3 and KS4 (Kyle *et al.*, 2011), KO (Ponomareva *et al.*, 2004), WPL2, WP6, WP5, WP9 , SR5 (Derkachev *et al.*, 2020), Rauchua (Ponomareva *et al.*, 2013).

Volcanic source	Tephra ID	Eruptions
Ksudash Calderas	KS3 and KS4	~ 6.4 resp. ~ 8.8 ka
Kurile Lake Caldera	KO	~ 8.4 ka
*Opala Volcano	WPL2 and WP6	~ 76 resp. 97 ka
*Gorely Volcano	WP5 and WP9	~ 80 resp. 125 ka
*Shiveluch Volcano	SR5	~141 ka
*Karymsky Volcanic Centre	Rauchua	~ 177 ka

3. Study Site and Project Aims

3.1 Previous Fieldwork

Sediment core SWERUS-L2-29-GC1 (hereafter referred to as 29-GC1) presented in this study was collected with Swedish IB *Oden* in September 2014, during the 90-day SWERUS-C3 (Leg 2) expedition. Leg 1 and 2 of the expedition started/ended in Tromsö, Norway (spanning from July 5th to October 3rd), with rotations in Burrow, Alaska. The 4.66-meter-long core was collected with a gravity corer from an 824 m water depth, and was split lengthwise and described onboard. Physical property measurements were carried through (bulk density and magnetic susceptibility) with a Geotek multi-sensor core logger. The core was later stored in a refrigerated storage (4°C) at the Department of Geological Sciences, Stockholm University. (West *et al.*, 2021; Bolin Centre for Climate Research, 2024)

3.2 The Lomonosov Ridge

Core 29-GC1 was retrieved from the southern end of the Lomonosov Ridge (LR) at 81.299356°N 141.78255°E off the Siberian shelf, Fig. 5a (Jakobsson *et al.*, 2016). The LR is a 1500-km-long ridge that divides the Arctic Ocean into the Eurasian and Amerasian basins. It extends from north of Greenland towards the Siberian continental margin, north of the New Siberian Islands, where minimum ridge depths vary from ~650–1400 mbsl. (Jokat *et al.*, 1992) Core 29-GC1was collected from the steeper lee side off the ridge, facing the Amundsen basin (Fig. 5b and 5c). A Chirp sonar sub-bottom profiler sampled undisturbed acoustically stratified sediments, deposited on top of an ice-scoured surface at the sampling site. Multibeam data from the core location have reviled two-sets of parallel streamlined submarine landforms interpreted as mega-scale glacial lineations (MSGL), extending diagonally from the Makarov Basin into the Amundsen basin (N and NW), Fig. 5c. (Jakobsson *et al.*, 2016)

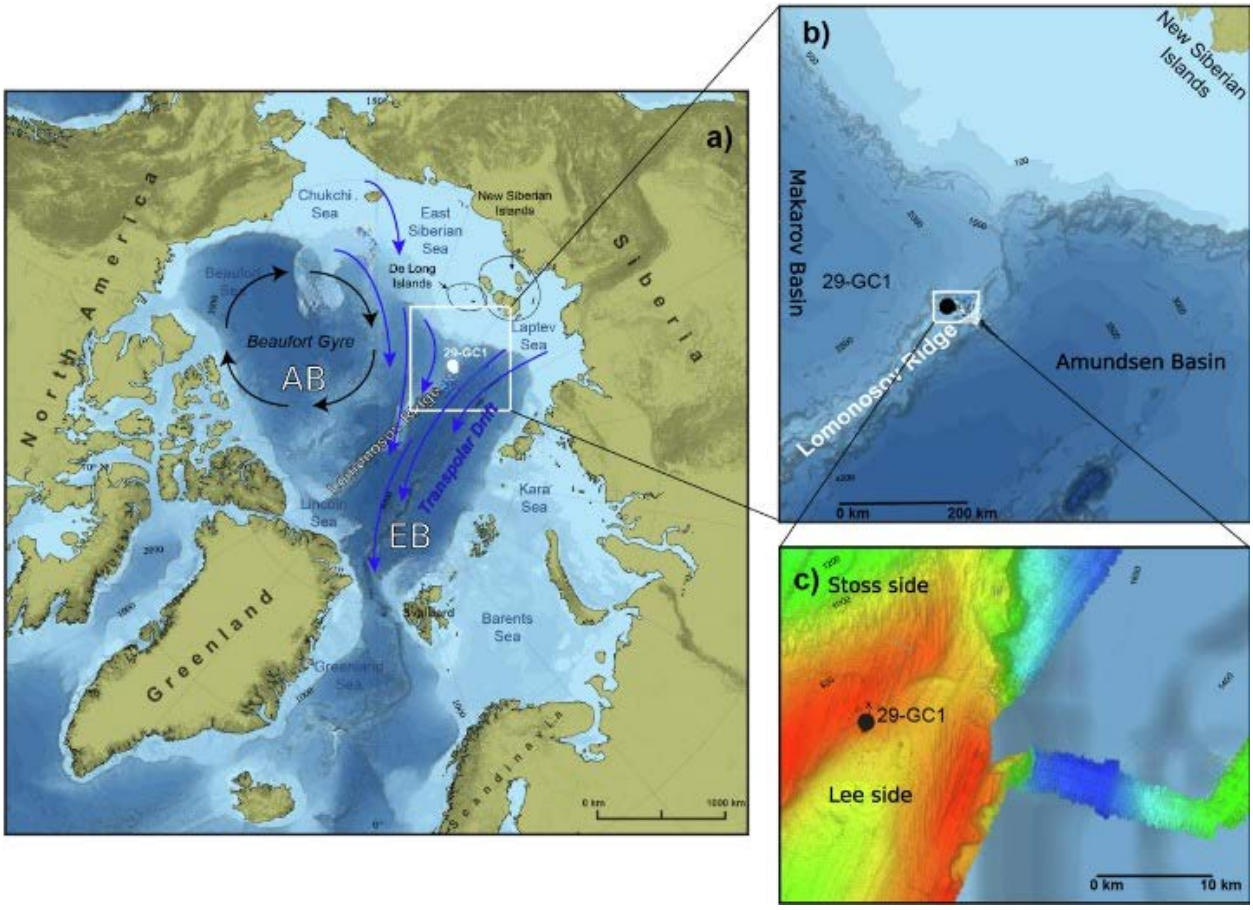

Fig. 5. Study site adapted from West *et al.*, (2021). **a)** Core location on the southern LR and dominant ocean currents. Black and blue arrows illustrate the Beaufort Gyre and Transpolar drift. Abbreviations: AB=Amerasian Basin and EB=Eurasian Basin. **b)** Detailed core location. **c)** Bathymetric highs, core location on the Lee side of the LR ridge.

3.3 Lithology and Stratigraphy

Core 29-GC1 mainly consist of light to dark brown sediments, that shifts into a grey layer at the bottom of the core. In a recent study published by Alatarvas *et al.*, (2022), four samples from the base of the core were analyzed for heavy mineral assemblages (marked A-D in Fig. 6a). Sample B-D were identified as diamict layer, that was overlain by a light brown silty clay observed in sample A (4.31 meters below seafloor (mbsf)). The grey diamict sequence was interpreted as an indication of an interglacial transition, or possibly

related to the ice-scoring of the LR ridge. In the top 5-cm of the core, calcareous microfossils were observed, indicating an Holocene age (Jakobsson *et al.*, 2016). Another calcareous fossil *E.huxleyi* was observed at 3.81 mbsf, in which possibly first appeared in Arctic Oceans during MIS 7 (O'Regan *et al.*, 2020). Core 29-GC1 haven't been influenced to any significant degree by downslope sediment transport such as e.g turbidites, or slope reworking, since it's lithology can be correlated to other cores on southern LR (Core *29-PC1* and Core *PS2757-8* (Appendix A: Table A1) and lack reoccurring erosional surfaces in sub-bottom data (West *et al.*, 2021).

Glacial/interglacial and stadial/interstadial setting can be interpreted with the use of proxy data, previously have wet bulk density, magnetic susceptibility, Manganese and Zr/Rb profiles been collected on Core 29-GC1, Fig. 6b. Generally, glacial deposits are; poorly sorted (i.e high bulk density), contain less magnetic minerals, abundant in sand and coarse silt-fractions (high Zr/Rb ratios) and contain low amounts of Manganese content (caused by e.g stagnant deep waters and low riverine input from the Siberian Shelf). Interglacial deposits are often well-sorted, rich in clay and deposited in more oxygenated deep waters, and will therefore (ideally) exhibit the opposite trends. (Vanderaveroet *et al.*, 1999; Dypvik *et al.*, 2001; Löwemark *et al.*, 2008)

3.4 Previous dating attempts

A relative mark for the MIS 6/5 transition was first assigned to Core 29-GC1 just above 4 mbsf by correlating physical data of magnetic susceptibility and bulk density to three additional cores collected along the LR; *Core 96/12-1pc* (central LR), *32-GC2* (central LR) and *PS2757-8* (southern LR) (Jakobsson *et al.*, 2016). This mark thereby suggested that the bottom of Core 29-GC1 could be traced back to early MIS 6. In a more recent study two datasets of numerical dates were obtained from an optically stimulated luminescence (OSL) dating on Quartz and Feldspar grains sampled from Core 29-GC1. These results provided two new scenarios for what MIS stage the bottom of the core could extend to, which will be further evaluated in this study.

3.5 Project Aims

In this study a tephra profile is collected on Core 29-GC1 (between 1.06-4.66 mbsf (Fig. 6a)), to investigate if peaks of the explosive Old Crow and Rauchua events have been preserved on the southern LR. This will be done by estimating cryptotephra concentrations and document shard morphology observation. The shard concentration profile will then be compared against the two age-depth Models derived from West *et al.*, (2021), with the aim of evaluating if Quartz dates or Feldspar dates are more likely applied to the studied interval.

Model 1 traces the core base to early MIS 5 (~ 110 ka BP) and if the Quartz-OSL dates are correct, then neither the Old Crow or Rauchua isochrons will be present in the studied interval (Fig. 6c). A background concentration of reworked Old Crow shards would likely be observed from the core base (i.e early MIS 5) and up (e.g Reyes *et al.*, 2022). Model 2, will test whether Feldspar-OSL dates could be correct, possibly tracing the core base back to the MIS 7/8 transition (~250 ka BP). This would potentially include both the Old Crow and Rauchua isochrons, with a Rauchua peak ~3.1 mbsf, followed by an Old Crow peak ~2.75 mbsf. Since geochemical fingerprints of potential shard peaks are not collected for this thesis, the results will only be able to distinguish which Model is 'more likely' or 'less likely'.

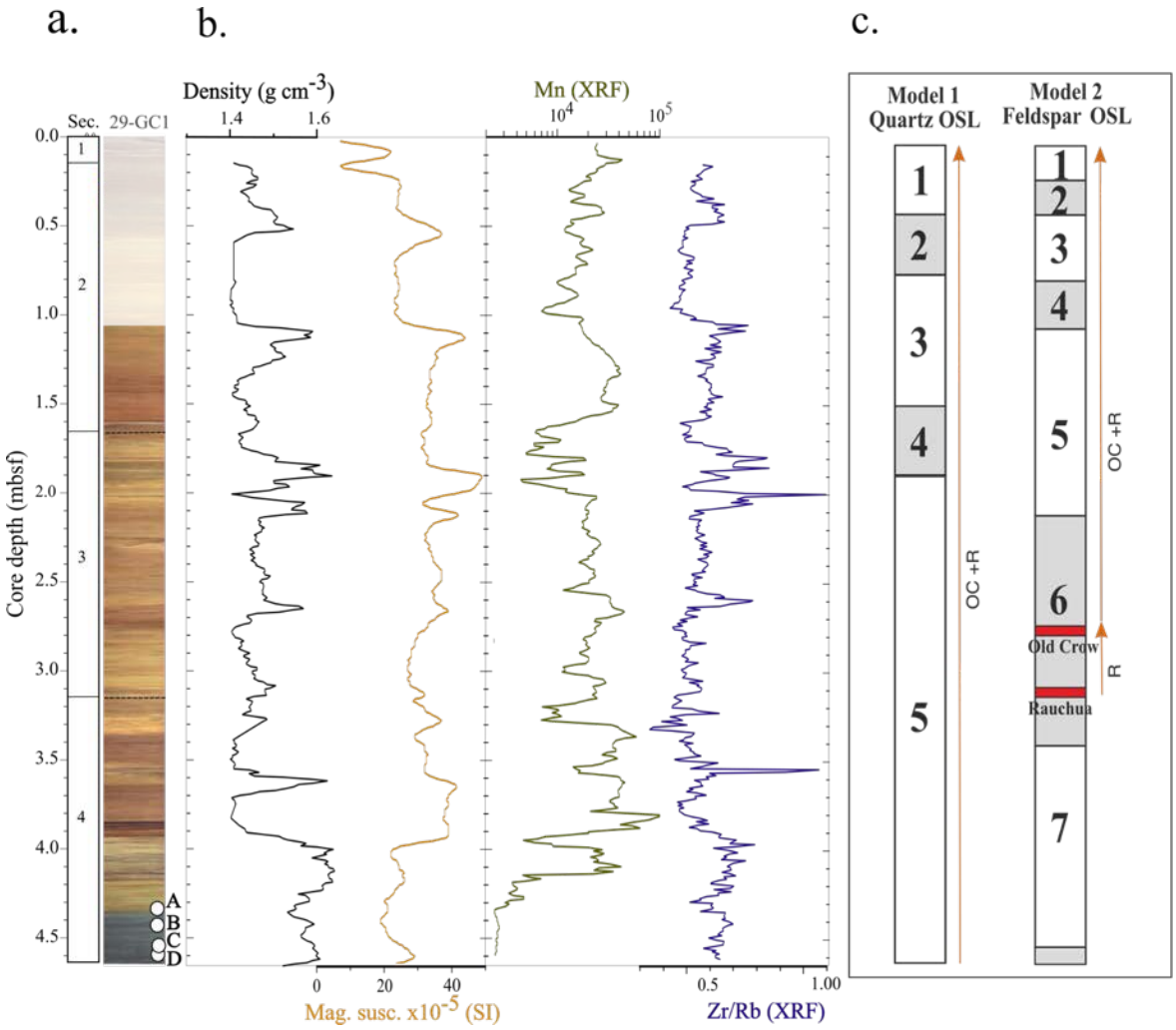

Fig. 6. **a)** Section depths and composite core image of Core 29-GC1, highlighted image corresponds to the studied interval for this project: 1.06-4.66 (mbsf). Samples for heavy mineral assemblages marked at core bottom; A = 4.31, B = 4.43, C = 4.55 and D = 4.62 (mbsf) (Alatarvas *et al.*, 2022). **b)** Previous obtained data of geophysical and elemental proxies, plotted downcore, data from (West *et al.*, 2021). Black: Bulk density (g/cm^3). Yellow: Magnetic susceptibility (SI x 10^{-5}). Green: Manganese counts from XRF (logarithmic scale). Blue: Zr/Rb element ratio from XRF. **c)** OSL age-depth models with Quartz and Feldspar dates, Old Crow and Rauchua events marked in red.

4. Materials and methods

4.1 Laboratory Work

Tephra extraction techniques can vary depending on targeted eruption and type of sampling material (Davies, 2015). In this study, cryptotephra subsampling and extraction procedures have been adapted from those described in; (Bennett *et al.*, 1992), (Turney, 1998) (Blockley *et al.*, 2005) and (Abbott *et al.*, 2018b), with the purpose of calibrating methodologies to; the unique arctic environment, rhyolitic shards and previously collected data on Core 29-GC1.

The aim of this tephra analysis was to isolate potential glass shards from the host material through a series of steps described below, in order to produce sample slides of unaltered glass shards suitable for calculating tephra concentrations and making morphology observations. Since cryptotephra shards can't be detected

with the naked eye, an initial low-resolution subsampling was made, consisting of 10-cm thick sediment samples (depth-wise). The initial 36 samples were prepared in the lab through a series of steps described below and optically analyzed under a microscope, this process was then repeated for one sample that was selected for a high-resolution resampling following marine tephra-isochrone criteria described by Abbott *et al.*, (2018). A schematic illustration of the quantification of shards can be seen in Fig. 7, with each step described further in detail below.

(1) The initial 10-cm low resolution subsampling was made between 106 cm and the bottom of the core at 466 cm on the Archive half of core 29-GC1 (Abbott *et al.*, 2018b), to target the Old Crow (159 ka) and Rauchua (177 ka) eruptions. Each section was unpacked and carefully scraped in order to remove potential contaminants from the upper surface. The intervals were marked in 10 x 1 x 0.5 cm sections (L x W x D) to obtain a wet sediment volume (ws) of approximately 5 cm^3. A total of 36 samples were collected and transferred into depth-labeled sampling bags (Lab ID in Appendix B: Table B1), followed by extraction procedures described below. For the second 1-cm resampling (Fig.7: step 7) of the selected interval (*Sec. 3: 70-80 cm*) 12 samples of 5 cm^3 (ws) were collected, Lab ID in Appendix B: Table B2 (Abbott *et al.*, 2018b). This included one additional cm at the top and bottom of the interval to exclude the possibility of an overlapping peak. These samples were homogenized and divided in half in order to create a primary and secondary sample. Primary samples were weighed before sample preparation, and secondary samples were stored in a refrigerator for potential future EPMA-analysis.

(2) Pre-treatment of tephra samples was initiated with removal of organic matter and disaggregation of clay-clumps using a strong acid. Samples from the first subsampling were transferred to 80 ml beakers and disaggregated in 30 ml (10%) hydrogen peroxide (H_2O_2) in room temperature (Bennett *et al.*, 1992) and left for 2h in an incubator until the reaction ceased. A few samples had a stronger reaction than expected, so Ethanol was added in drops to restrain the reaction. The high-resolution samples were disaggregated in 20 ml of a weaker (3.3%) hydrogen peroxide because of their smaller sample size and left to dissolve for 1h.

(3) Samples were sieved through grain-size fractions of 25-100 µm diameters to isolate the sediment fraction in which cryptotephra could be present. A wire mesh was used for the upper limit and a nylon mesh for the lower. The nylon mesh was changed regularly to avoid loss of finer particles within the wanted fraction. The remaining material was transferred to a depth-labeled test tube. When sieving each sample through the 100 µm fraction, grains larger than ~ 4 mm was documented as potential IRD indicators.

(4) The 25-100 µm grain size fraction was further isolated with sodium polytungstate (SPT) - a heavy liquid with a specific gravity, through a series of centrifuge steps. The test tubes were first filled to the 4 ml mark with 2.3 g/cm^3 SPT, used to clean the samples from lighter compounds (< 2.3 g/cm^3) which are often of biogenic origin. The samples were then stirred, for total agitation, and centrifuged during 15 min in a *VWR MEGA STAR 1.6* using the settings; 2500 vpm and 9:4 acceleration (where setting 9 equals maximum acceleration in the start and 4 generates a gradual break-in). A gradual decrease in acceleration helped the lighter densities to separate even further from the sample. The residual float was poured out (without removing the packed material in the bottom of the test tube), and additional 2.3 g/cm^3 SPT was added to the 4 ml mark. A total of three centrifuges was done with the lighter SPT, followed by three 'cleaning' centrifuges (settings: 15 min, 2500 vpm, 9:9) where the samples were centrifuged in distilled water in order to remove the remaining SPT. The same process was then repeated with the addition of 2.5 g/cm^3 SPT, used to clean samples from heavier compounds (>2.5 g/cm^3) often of a minerogenic origin. This time the remaining float was poured in a new test tube (the tephra sample), labeled with the sample name and an X to avoid

cross contamination. This extraction was now in the density fraction of 2.3 - 2.5 g/cm^3, that corresponds to the density interval of rhyolitic glass shards. The samples were centrifuged and extracted three times, followed by three cleaning centrifuges of the tephra samples. (Turney, 1998; Blockley *et al.*, 2005)

The high-resolution samples were subjected to an additional step before mounted on a microscope glass. A tablet with known amounts of *Lycopodium* spores was added to each tephra sample together with 3 ml of a weak HCl solution for dissolution off the tablet matrix.

(5) The extraction float was dropped on a heated microscope glass with a pipette. When the sample had dried out it was stirred with Canada balsam and a slide cover was pressed on top. This was then followed by microscopy work, step (6). (Turney, 1998)

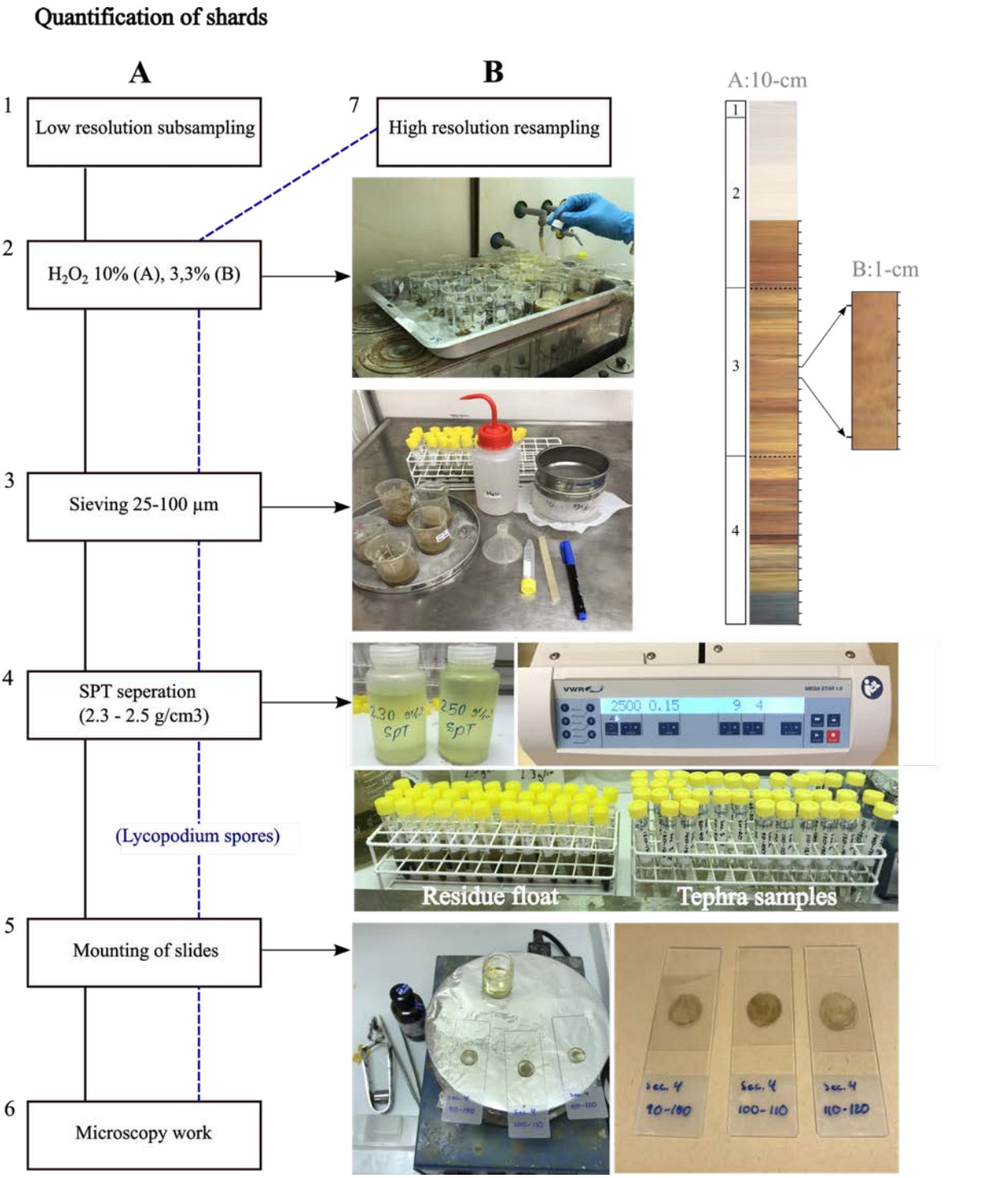

Fig. 7. Schematic illustration of the shard quantification process. **A**) Preparation process for the 36 low-resolution samples (step 1-6). In step 6, glass shards were manually counted, and a suitable high-resolution sample was selected. **B**) Repeated preparation process for the 12 high-resolution, with an additional *Lycopodium* spore step. **Pictures**: **Step 1** – Figure of sampling intervals. **Step 2** - Addition of hydrogen peroxide for dissolution of organic material. **Step 3** - Sieving and transferring samples to test-tubes. **Step 4** - SPT used for the density separation of rhyolitic shards and centrifuge settings, the final extracted tephra samples (right) after the last density separation step from samples to the left. **Step 5** - Mounting of the tephra sample on heated microscope glasses. Modified from (Davies *et al.*, 2005).

4.2 Microscopy work

Using an optical microscope (*LEICA*), the amount of glass shards in each sample was manually counted. Glass shards were identified using the following morphology criteria: colour – (transparent for rhyolitic shards), moderate to high relief, shard appearance and texture - (i.e sharp edges, vesicles, micro-inclusions and junctions) and isotropic characteristics - (turn black when a polarization filter is applied) (Lowe, 2011; Larsson, 2022). Beside counting glass shards of potential tephra, 'uncertain' shards were also counted in a separate category. Some particles could appear to exhibit several of the listed criteria but factors such as background noise in a few samples (high amounts of minerogenic material that caused overlapping between particles), small particle sizes and mounting related issues (air bubbles in Canada balsam or aggregated material) could make identification more difficult. Some glass shards were photographed with a digital camera from Leica Microsystems together with the Leica LAS EZ, for morphology documentation. When counting glass shards in the microscope from the high-resolution samples, the *Lycopodium* spores were also counted. When 300 spores had been counted, the shard concentration was estimated according to Equation 1:

$$c = l \cdot \frac{a}{bd} \quad (1)$$

where a is the number of counted shards, b is the number of counted *Lycopodium* spores, d is sample weight in g (wet weight in this case) and l is the total amount of spores in the tablet. (Gehrels *et al.*, 2006)

4.3 Comments on sample preparation

A method for rhyolitic glass shard extraction in marine sediments, specifically targeting Arctic origin hasn't been proposed. Abbott (2018) presented a method for analysis procedures adapted to marine sediments with high minerogenic content in the North Atlantic. In previous studies from the Arctic, removal of organic material has been done by freeze-drying (e.g Pearce, 2017; Ponomareva, 2018). This method ensures that the glass shards remain chemically unaltered which is important for EPMA analysis (Blockley et al. 2005). This procedure also allows for tephra concentrations being calculated by dry weight and could result in more exact estimations if e.g organic content of the sediment is high, and results would also be easier to compare with previous publications. Freeze-drying is however a time-consuming process when preparing large amounts of samples (Turney, 1998). Since these samples weren't prepared for a geochemical analysis, and to save time, removal of organic material was decided to be done with hydrogen peroxide. Tephra concentrations were decided to be reported per wet sediment (ws) volume and (ws) weight. Organic matter removal is often followed by the addition of (10%) hydrochloric acid (HCl) overnight for the dissolution of carbonates, before sieving. A HCl treatment was skipped since Core 29-GC1 lacked calcareous micro-fossils in the studied interval (West *et al.*, 2021).

4.4 Rationale for selecting an interval for high resolution sampling

After initial subsampling the decision to select a core depth interval for high-resolution (1-cm) sampling depended on peak versus background concentration, peak discreteness and shape, and the presence of IRD. (Abbott, 2018) After the low-resolution sampling, two core sections were considered for a high-resolution resampling: *Sec 3: 70-80* and *Sec. 4: 110-120*. Sample *Sec. 3: 70-80* had high shard concentrations and a distinct peak with low background concentrations above, additionally no IRD was located near this level. The core interval located at *Section 4: 110-120* cm had a minor peak surrounded by a few elevated intervals in the bottom of the core, since shard concentrations weren't as high as in *Sec. 3: 70-80* the previously and IRD was located just above, this interval was ruled out.

5. Results

5.1 Glass Shard Concentrations

No visible ash layers were detected in the studied interval of Core 29-GC1, although cryptotephras were identified in nearly all of the low-resolution samples, see Fig. 8b. The uncertain shards appeared to mirror the 'certain' shard signal in a majority of the samples. This could mean that 'true' shard concentrations are higher than what the certain signal indicates. The ratio between the two does however increase towards the core bottom in the low-resolution profile (Fig. 8b), explained by background noise related to larger volumes of minerogenic material that remained in these samples even after extraction, Appendix C - (Fig. C1 and C2). Aggregated materials in the high-resolution samples (Fig. 8c) also caused elevated uncertainties. Since the 'uncertain' signal doesn't affect the results to any significant extent (e.g places peak interval at different depth), only the 'certain' shard results will be presented in more detail below.

5.1.1 Tephra Peak

The sample interval 236 - 246 cmbsf (i.e *Sec. 3:70-80 cm)* had the highest amount of glass shards out of all low-resolution samples, with 39 shards/5cm^3 (ws) (Fig. 8b). Above this peak an 80 cm segment (between 156-236 cmbsf) was observed with very low shard amounts, ranging from only 0-3 shards/sample. Below the peak, a 'tail' followed with three samples of moderate concentrations (12-13 shards/sample). The peak interval had; a discrete shape, high shard counts, no potential IRD observations and prevailed over the potential background signal. These characteristics are also used for describing single depositional events that are related to primary ashfalls in the marine environment (Lowe, 2011; Abbott *et al.*, 2018b), therefore high-resolution data was collected from this interval as well, see Fig. 8c.

A moderately discrete peak was seen in interval 236-238 cmbsf, stretching over two samples (*Sec 3: 70-71 cm* and *Sec.3: 71-72 cm*) with estimated concentrations of 229 and 235 shards/g (ws) respectively. Overlaps between concentration peaks in high-resolution samples is common for marine settings, and may be explained by some type of reworking mechanism (Lowe, 2011). A larger grain (Fig. 9c) was also discovered in the lowermost interval 246-247 cmbsf (*Sec. 3 80-81*). The uppermost and lowermost intervals both contained lower concentrations than the rest of the profile (with one exception in interval 240-241 cmbsf).

5.1.2 Minor Lenses

A majority of the samples that contained tephra appeared to be in the count-range of 5-14 shards/sample. Intervals with low shard amounts that appear to be reoccurring could be caused by background concentrations of reworked shards, often sea-ice deposited (Griggs *et al.*, 2014). Two intervals contained >15 shards/sample, and marked minor peaks, or lenses in the profile. Lens 1 (L1) was located in interval 136-146 cmbsf (*Sec. 2: 120-130 cm*), in a 50 cm segment (between 106-156 cmbsf) of potential background signal. Lens 2 (L2) was discovered near the bottom of the core at 416-426 cmbsf (*Sec: 4 110-120* - Lens 2) located in a longer 80 cm segment (between 386–466 cmbsf) of what could be the background signal. Just above Lens 2, larger grains collected from the >100 µm coarse fraction were identified in two samples (interval 396-416 cmbsf, Fig. 9a-b).

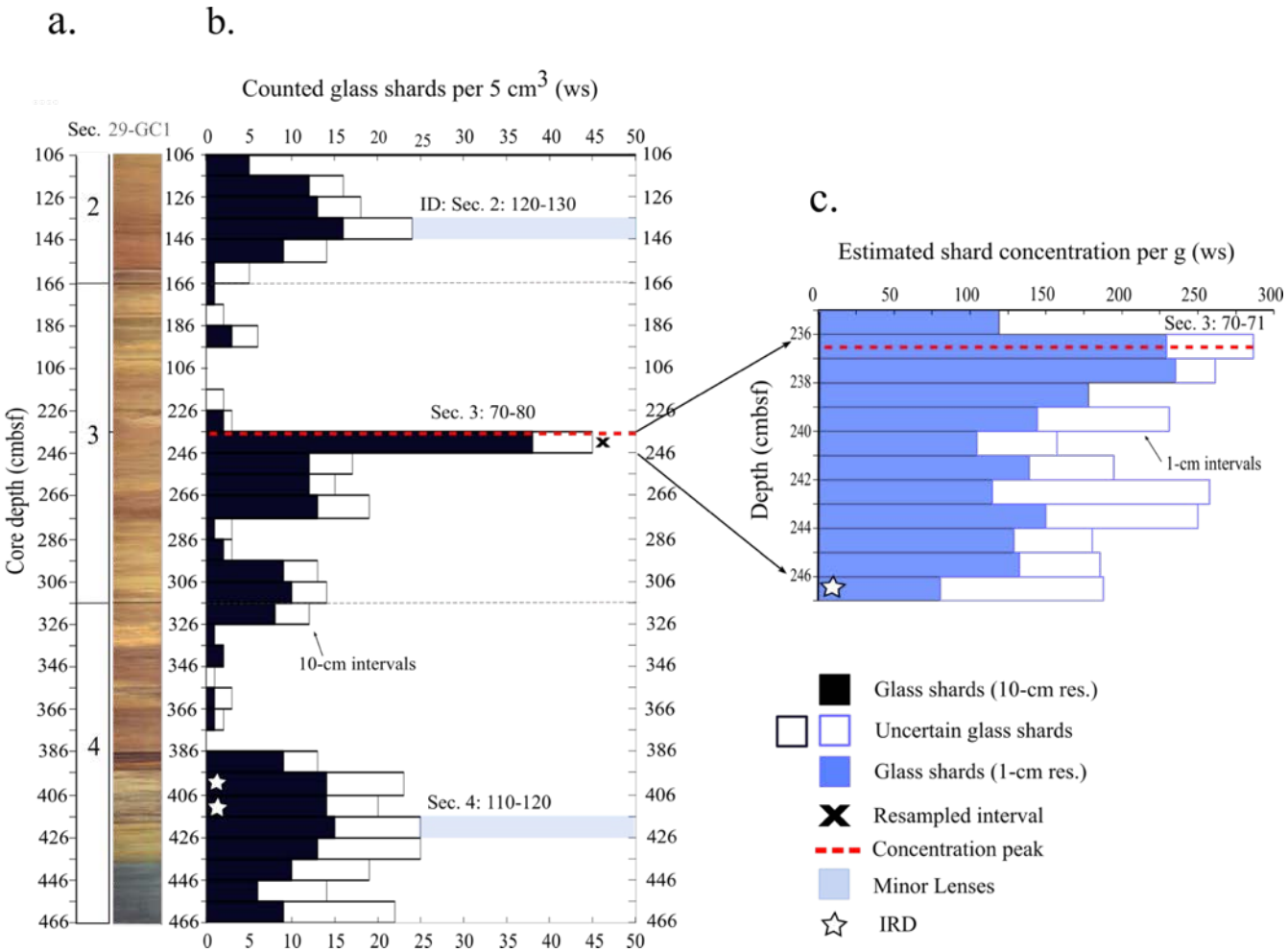

Fig. 8. Glass shard concentrations from low- and high-resolution sampling. See legend for colour interpretation. **a)** Section depths (cmbsf) and composite core image of Core 29-GC1. **b)** Counted glass shards per 5 cm^3 (ws) from low-resolution samples. Peak interval 236-237 cmbsf. **c)** Estimated shard concentration per g (ws) from high-resolution samples.

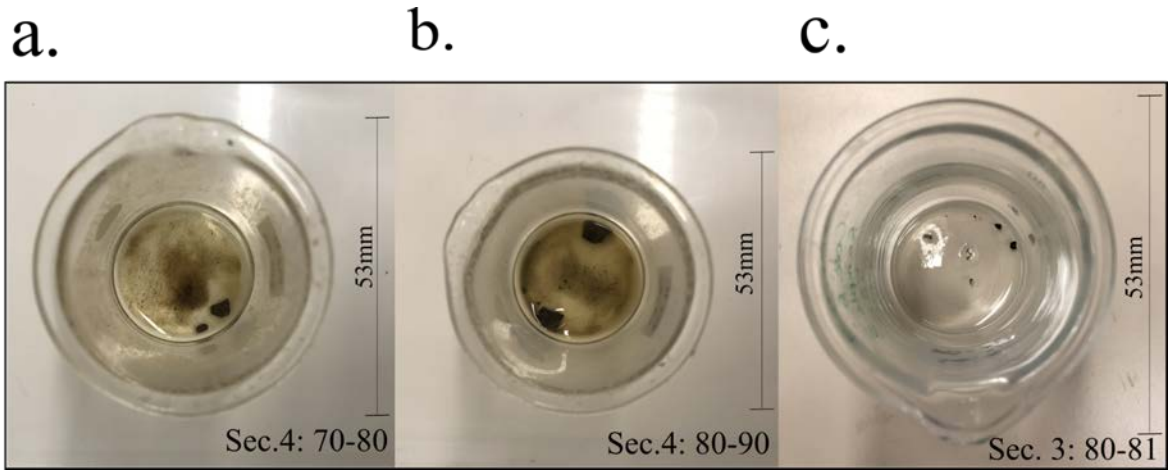

Fig. 9. IRD discovered in the studied interval. **a)** Interval 396-406 cmbsf. **b)** Interval 406-416 cmbsf. **c)** Interval 246-256 cmbsf.

5.2 Shard Morphologies

5.2.1 Morphology Types Identified

A range of different shard morphologies were identified in the studies sequence, see Fig. 10. All shards were transparent, indicating a rhyolitic composition (Lowe, 2011). Morphologies could be divided into five different categories. Type (1) consist of platy, blocky shards with some junctions. Type (2) are blocky shards with larger vesicles. Type (3) contain shards that are blocky and microvesicular, referred to as *pumiceous* (McLean *et al.*, 2018) .Type (4) are fibrous, microvesicular and cuspate, e.g angular curved edges or bubble-wall appearance. Finally, type (5), cuspate elongated shards with tear-dropped vesicles, a shape that may indicate direction of flow (Enache *et al.*, 2006). These observations could indicate that deposits from different eruptions are preserved in the sediments, although a vast majority of the identified shards were vesicular. Microvesicular shards appeared to be more abundant towards the bottom of the core, and platy shards occurred sporadically throughout the studied interval.

5.2.2 Shard Morphology in Peak

The main shard morphology identified in the peak sample, *Sec.3: 70-80*, were mainly of a vesicular character including both type (3) and (4), even though some platy shards of type (1) also were observed, Fig. 11a. Some vesicles contained inclusions, Fig. 11b. Inclusions in cryptotephra shards are commonly microlite-inclusions (e.g McLean *et al.*, 2018), often composed of plagioclase or Fe-Ti oxides (Platz *et al.*, 2007). Shards with inclusions were identified in some other samples as well, although not to the same extent. This is not a characteristic that's been described for either the Old Crow or Rauchua shards.

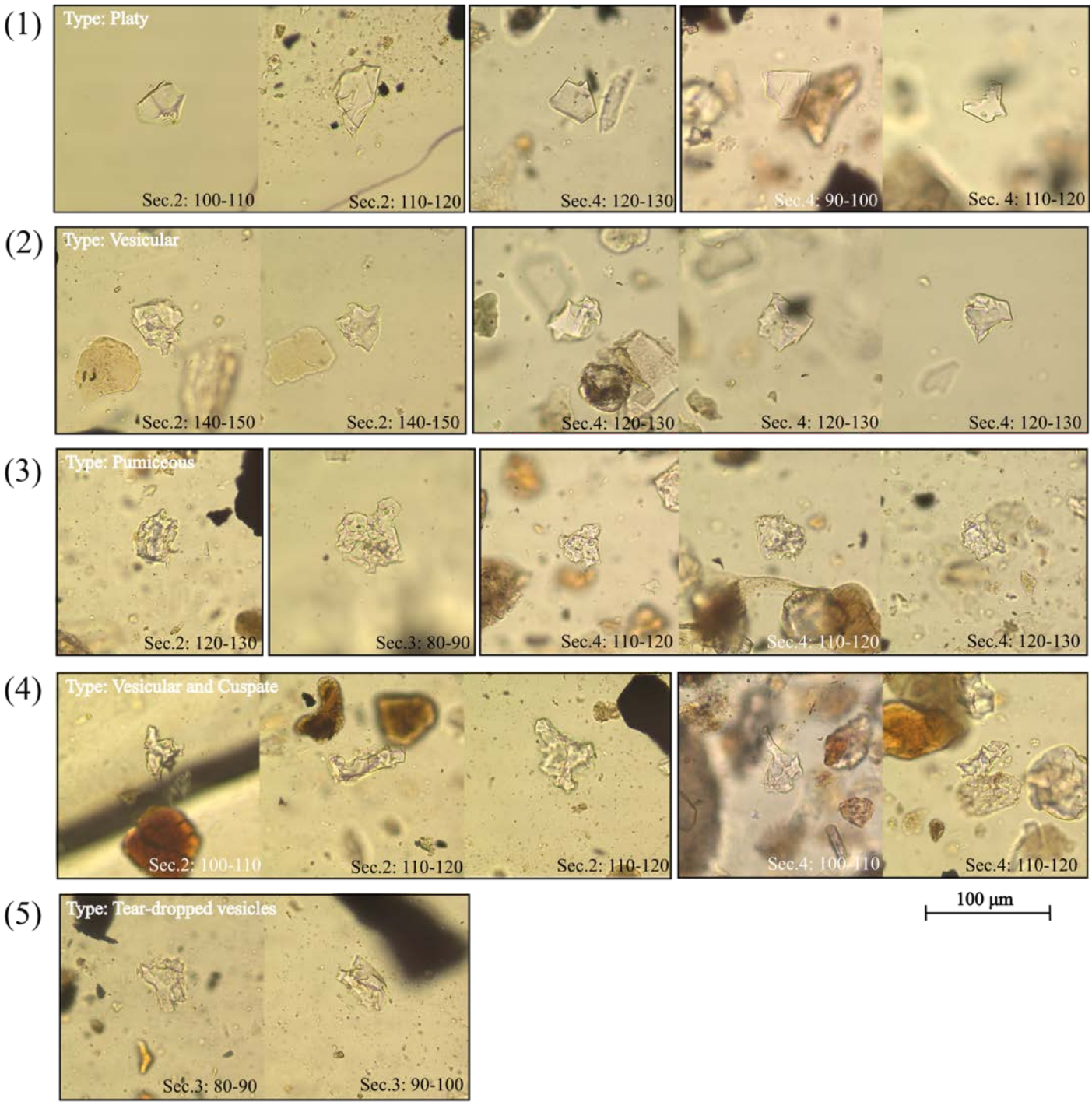

Fig. 10. Identified morphologies in the studied sequence. **a)** Platy. **b)** Vesicular. **c)** Pumiceous. **d)** Microvesicular and Cuspate **e)** Tear-dropped vesicles.

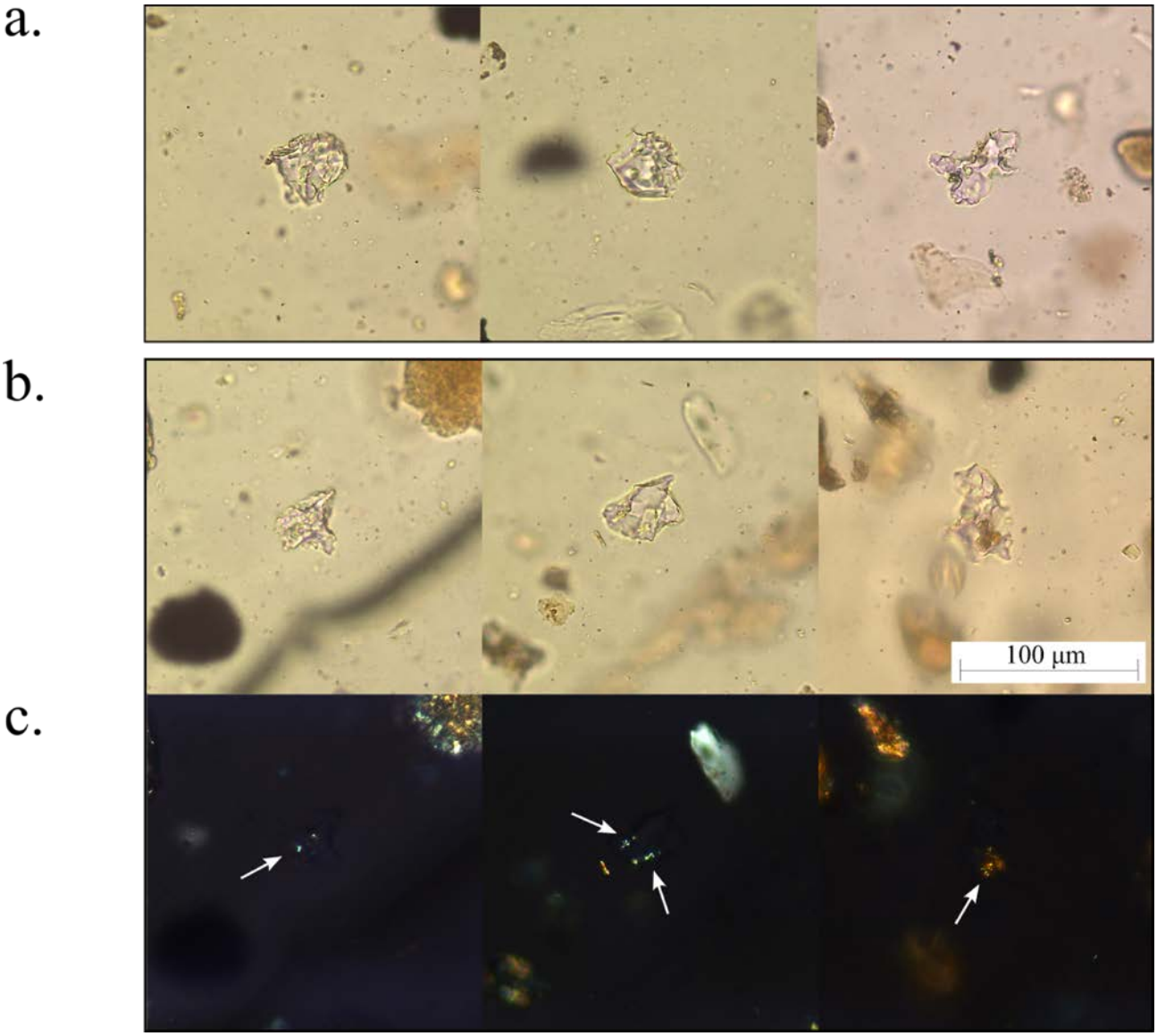

Fig. 11. Identified morphology types in peak interval 236 - 246 cmbsf (*Sec.3: 70-80*). **a)** From left to right: type (3)-pumiceous, type-(3) pumiceous, type (4) Vesicular and cuspate. **b)** Pumiceous, and bubble-wall shards. **c)** Same view as in (b) with applied polarization filter, arrow point towards possible microlite inclusions.

5.3 Implementing Tephra Signal in Age-Depth Models

5.3.1 Comparing the Tephra Signal to Model 1

In Model 1, Quartz-OSL dates traces the bottom of 29-GC1 to early MIS 5 (~110 ka), background signals of both volcanic events would therefore be anticipated to be observed in the tephra signal as a gradational upward tail (Fig. 12e). A segment with elevated shards was identified in the bottom of section 4, although not displaying the preferred trend. A trend in decreasing shard counts wasn't seen throughout the studied sequence either. Shard morphologies in this segment, and throughout the whole core were mainly clear and vesicular, characteristics that are somewhat similar to those described for the Old Crow and Rauchua shards. According to Model 1 the identified peak concentration was deposited during late MIS 5, the L2-segment would be traced to early MIS 5, and the L1-segment to the MIS ~3/4 transition.

5.3.2 Comparing the Tephra Signal to Model 2

Model 2 (Feldspar-OSL) suggests that the base of the core dates back to the MIS 7/8 transition (~250 ka), potentially including both the Rauchua peak at ~310 cmbsf and the Old Crow peak ~275 cmbsf. The Rauchua event aligns with a 30 cm segment (between 296-326 cmbsf) with very low shard counts (~10 shards/sample). Below the peak concentration observed in this study (in which post-dates both events with its late MIS 6 placement) a 'tail' followed (described under *5.1.1 Tephra Peak*), and the Old Crow event aligned with the lowermost of those samples. The L2-segment dates back to MIS 7, and the L1-segment to MIS 4.

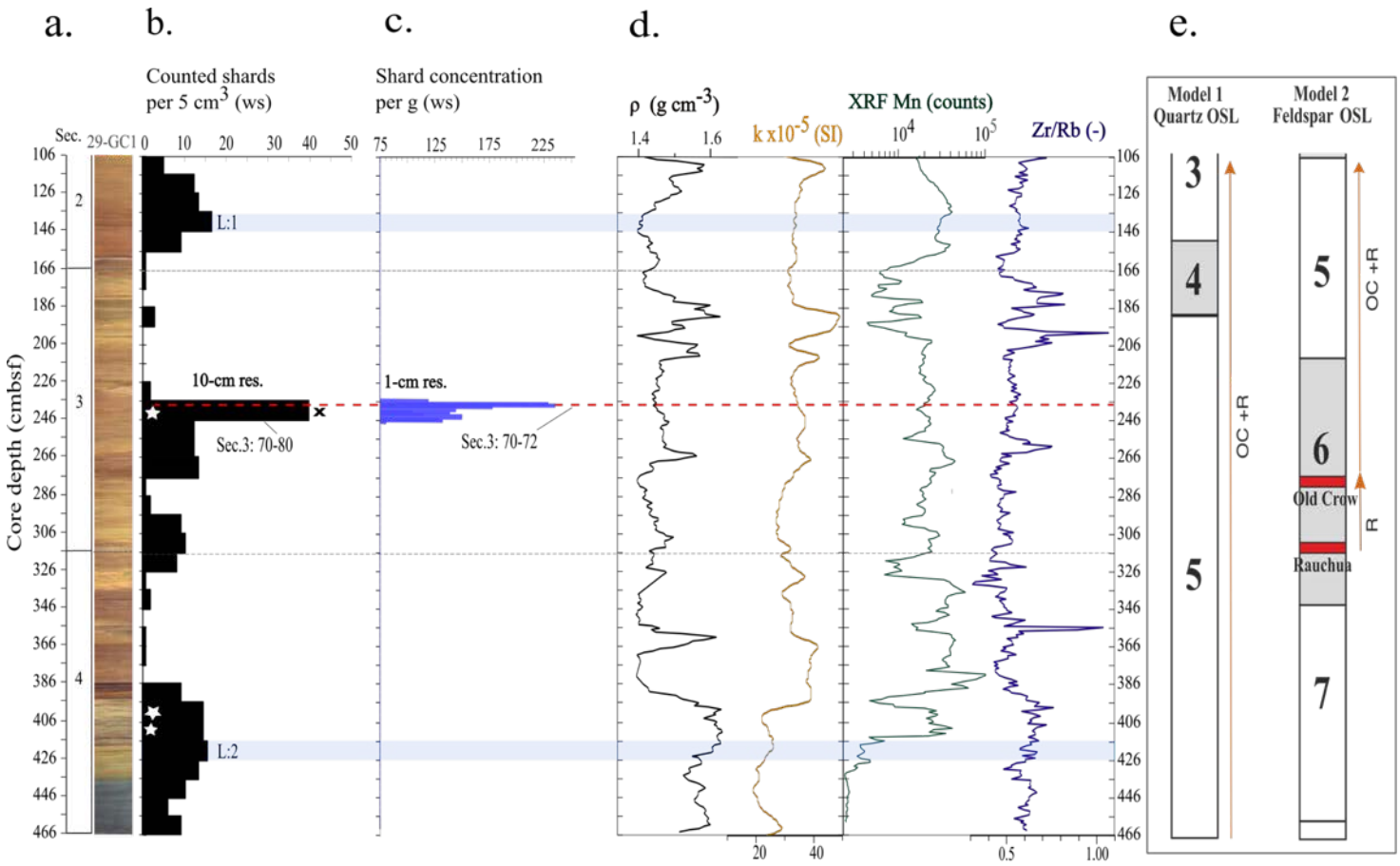

Fig. 12. Tephra results combined with previous data and age-depths models. **a)** Section depths (cmbsf) and composite core image of Core 29-GC1. **b)** Counted glass shards per 5 cm^3 of wet sediment from low-resolution samples. **c)** Estimated shard concentration per g of wet sediment from high-resolution samples. **d.)** Previous obtained data of geophysical and elemental proxies, plotted downcore. Black: Bulk density (g/cm^3). Yellow: Magnetic susceptibility (SI x 10^{-5}). Green: Manganese counts from XRF (logarithmic scale). Blue: Zr/Rb element ratio from XRF. (West *et al.*, 2021) **e)** OSL age-depth models, Old Crow and Rauchua events marked in red.

6. Discussion

6.1 Shard morphologies on the Lomonosov Ridge

Within the studied interval of Core 29-GC1, cryptotephras with diverse morphologies were observed (Fig. 10), with vesicular shards being significantly more abundant than platy ones. Variations in vesicle size and shape may arise from the magmatic differentiation taking place during the evolution of the eruption or a sign of heterogenetic origin (Platz *et al.*, 2007). Although, comparing shard morphologies over long depth-intervals should be done with caution, considering the timescale of deposition. A mix of tephra's may be deposited on the seafloor through the continuous sedimentation of volcanoclastic materials of e.g sea-ice rafted or terrestrial derived deposits. Incorporating shards from smaller, older or previously undocumented eruptions at the site.

If similar morphologies are found within a constrained interval where shard concentrations also mark a discrete peak in the tephra-profile, chances of them being related to the same source vent increase (e.g Katoh *et al.*, 2000). In the observed peak shards morphologies were mainly pumiceous and bubble-wall, with cuspate shapes (Fig. 11). Some shards contained potential microlite inclusions in which occurrence was more abundant in this interval. Microlites are usually derived from more intermediate magmas, and crystallization during progressive accent may be induced as the magma degasses. Plagioclase microlites are often <10 µm long, and needle-shaped. (Platz *et al.*, 2007) Those identified in Fig. 11a-b, could match this description, although not displaying an ideal needle-shape. If these shards are related to the Old Crow or Rauchua events, they may have been derived during a later stage of eruption. An example of a tephra that previously have been described with microlite inclusions is the SR5 tephra, derived from the Shiveluch volcano (~141 ka), Table 2 (Ponomareva *et al.*, 2015).

In literature, the morphology of both the Old Crow and Rauchua shards are described very similarly (e.g clear shards with bubble wall fragments), and this type of morphology was observed throughout the core. A majority of the cryptotephra that will be able to reach this distal region can however be assumed to have this type of morphology, since these are typical characteristics of very explosive events. Even secondary deposits from e.g terrestrial input may have a prevailing rhyolitic composition (that clear vesicular shards often tend to indicate) since their high silica content make them resistant to weathering. Shard morphology may also vary with distance from the source vent, and it's unclear from which localities the morphological descriptions of Old Crow and Rauchua tephras were collected. Considering this, it's still likely that the identified shards originate from the North Pacific arcs (Fig. 4), being the closes volcanic source able to generate these types of eruptions. Transport and deposition, whether primary or secondary, to the coring site where 29-GC1 was collected may therefore have extended more than 3000 km from the original source vent(s).

6.2 Primary or Secondary Transport

Primary ash-fall deposits, from single volcanic events may (if preserved), display very similar characteristics as single secondary depositional events in the tephra-profile. Even though a peak was identified (Fig. 8b), small variations in its morphology could indicate secondary transport e.g sea-ice or iceberg deposited, potentially incorporating several tephra deposits. Additionally, primary ash-fall deposits generally display

even higher concentrations (Abbott *et al.*, 2018). Although, its uncertain how a significant deposit of the Old Crow or Rauchua events would appear like in this distal region. The relative high background signal observed in the high-resolution profile, in combination with observations of larger grains in the lower interval (Fig. 8c; Fig. 9c) may indicate that the peak could have been related to an amplified background signal, caused by secondary transport. Sea-ice and iceberg rafted materials are more common during glacial phases or glacial-interglacial transitions (Darby *et al.*, 1997). A slowly decreasing density and increasing Manganese signal (Fig. 12d) might suggest a climatic setting where well-sorted sediments deposited in oxygenated waters. Therefore sea-ice deposition during a glacial-interglacial transition may have been more likely.

High background signals in the peak interval may also indicate that the horizon have been re-worked, through e.g bioturbation, intensified bottom currents during interstadials and/or turbidities. No evidence of bioturbation, or of macrofossil in general, have been reported in previous studies made on Core 29-GC1(e.g Hällgren, 2015; Jakobsson *et al.*, 2016; West *et al.*, 2021), nor have they been identified during this study. Therefore, this process is considered to have had an insignificant influence. Core 29-GC1, was collected from the steeper Lee side of the LR ridge (Fig. 5c) and slope mechanisms may influence the sedimentation process at least to some degree, although no evidence of larger turbidities have been identified in the core. This might take place on a smaller scale than resolution of the geophysical property profiles allows for.

Obtaining the geochemical signature of the peak would help determine whether this horizon is related to the Old Crow or Rauchua volcanic events, as well as distinguishing if shards were sea-ice or iceberg deposited.

6.3 Shard Deposition in Model 1

According to Model 1 the core base dates back to early MIS 5 (~ 110 ka) (Fig. 12e), and neither the Old Crow nor Rauchua primary peaks would be present in the sequence, although background concentrations of especially Old Crow shards would likely gradually tail upwards during early MIS 5 (e.g Reyes *et al.*, 2022). The L2-segment in the bottom of section 4 (386-466 cmbsf) could potentially reflect this background signal, although no upward decreasing trend was observed in this segment or throughout the core (Fig. 12b). Shard morphologies observed in the L2-segment were mainly vesicular with blocky or elongated shapes, could potentially be an example of the 'fluidal textures' that's been described for the Rauchua tephra. Shards matching the Old Crow description were also identified, although to a smaller extent. Considering that visible Rauchua ash layers have been identified along the Arctic Siberian coast, and sediment transport along the east Siberian Shelf, secondary deposits from this event may have had an advantage in reaching the southern LR, through e.g shard incorporation in sea-ice along the shore. In this Model, the background signal doesn't necessarily imply that the southern LR were subjected to a primary ashfall from any of these eruptions, even if the Quartz-based OSL age model would be correct.

The Quartz-based OSL age model indicates that the stadial stage of MIS 5d (~115-105 ka) represents the lower part of the core, followed by the interstadial of MIS 5c (~105-92 ka), stadial MIS 5b (~92-85 ka), and interstadial MIS 5a (~85-75 ka) (Fig. 1).

The stadial substage MIS 5d roughly constrains the L2-segment. Elevated bulk density, low magnetic susceptibility and increasing Zr/Rb values are observed. This could indicate that deposition of poorly sorted, coarser fractions was deposited, indicating sea-ice or iceberg deposition. Larger grains were also discovered during sample preparation (Fig. 9a-b, interval 396-416 cmbsf), and Hällgren, (2015) also highlighted that a grain >8 mm was discovered in a sample from this interval. Elevated Manganese levels towards the end of this stadial could indicate increased riverine input from Siberia and/or oxygenated bottom waters, possibly an effect of the interstadial transition into MIS 5c. The L1-segment is positioned close to the MIS 4/3

interglacial transition, which again might be related to increased sea-ice deposition, climatically imposed. If this is the case, reworking related to intensified bottom currents might have influenced this signal.

The interstadial MIS 5a is the interval in which the tephra peak is located in, and its downward tail of background noise. Open-water conditions is a crucial condition for the preservation of primary deposits. Tephra peaks recorded in interglacial or interstadial sediments could therefore have a higher probability of being related to primary events, although higher sea-levels might lead to a larger degree of delay during the oceanic settling. Both volcanic events took place during the MIS 6 glacial phase, with evidence of MSGL and ice-scoured surfaces at the site where the core was collected (Fig. 5), related to the mentioned ice shelf. In Model 1, the recorded tephra peak is observed in the later phase of MIS 5, which therefore could increase its reliability as a primary deposit. This type of reasoning may however be problematic, since the climatic regime might further be controlled by seasonal factors such as; increased sea-ice coverage during interglacial winters, open water conditions during glacial summers, atmospheric winds and precipitation patterns, (Lowe *et al.*, 2017) that may scatter or concentrate depositions from the tephra plume regardless of climatic setting. Additionally, poorly studied eruptions more closely related in time may have had an influence.

For example, the WP5 tephra was recently identified in core SO201-2-40 from the Bearing Sea, dated to a very explosive eruption ~80 ka, with a magnitude of 6.0 (Fig. 4, Table 2). Very little is known about this eruption, but if atmospheric conditions allowed for a partly northern depositional axis, it might have been possible for at least background concentrations of this event to reach the site, considering its calculated tephra volume of 10.49 km^3. Other MIS 5 tephra's >14 km^3 are WP7 (~ 103 ka) from the east volcanic front (i.e Opala and Karymsky belt) and WP9 (~ 125 ka), an older Gorely event. (Schindlbeck-Belo *et al.*, 2024) In Model 1, these explosive eruptions, in combination with Old Crow and Rauchua tephras, might have been an explanation to the variety of shards types that were identified.

6.4 Shard Deposition in Model 2

The Feldspar-OSL age model suggest a ~250 ka age for the base of 29-GC1, placing it at the MIS 7/8 boundary (Fig. 12e). The L2-segment is now deposited until late MIS 7, although the background signal in this case would be related to older Pleistocene eruptions (e.g Derkachev *et al.*, 2023 and Ponomareva *et al.*, 2023). In comparison to Model 1, the glacial-interglacial transition in the bottom might provide a better explanation for the deposition of the identified diamict sequence identified below ~ 4.31 mbsf (Fig. 6a).

The recorded tephra peak predates both volcanic events in this model and ends up in late MIS 6, considering the MSGL and ice-scoured surface identified in the sub-bottom data below Core 29-GC1, these conditions may not be favorable for the preservation of primary ash-fall deposits. The ice-grounding have been dated to ~140 ka (Jakobsson *et al.*, 2016), and this event could have diluted the shard concentrations if they were able to reach the seabed before it grew extensively. Entrainment in sea-ice would otherwise result in a delayed deposition, potentially where both the Rauchua and Old Crow tephra accumulated simultaneously on the seafloor as the iceshelf retreated, resulting in one high-concertation interval of reworked shards. Considering that the tephra peak almost pinpoints ~140 ka, this scenario may be unlikely since the oceanic settling would have been prevented by the > 1km thick icesheet. Since relative steady rates of change is observed in the geophysical and elemental proxy data, and no ice-scoured surface was observed at this depth, this model doesn't appear to align with the tephra signal or previous collected data. Model 2 is further limited by very low sedimentation rates.

During pre-treatment (Fig. 7: Step 2) with H_2O_2 a few samples in the bottom of sec. 4 were discovered to have stronger reactions than expected, suggesting a high organic content in these intervals. These samples coincide with a strong decline in magnetic susceptibility. In marine cores from the Norwegian Sea, a decline in magnetic susceptibility has been coupled with dilution of magnetic minerals, due to increased carbonate

deposition during the MIS 5e stadial (e.g Brendryen *et al.*, 2010). Maybe this decline in magnetic susceptibility could be linked the MIS 5e stadial in this profile as well, caused by e.g increased influx of carbonates in the bottom waters from the north Atlantic Ocean or from terrestrial sources. Increased input of organic matter during MIS 5e in combination with the enhanced presence of carbonates may be an explanation to why a stronger reaction could be observed.

It should also be mentioned that both the Quartz-based and Feldspar-based OSL dates have been calculated with a degree of uncertainty, which amplifies with core-depth in the OSL samples. The last ~0.5 m, in both models have additionally been derived through linear extrapolation. Some degree of uncertainty is expected in all age-models, in this case however, the range for Feldspar derived dates suggests that incomplete bleaching due to sea-ice rafting may have been a contributing factor, potentially generating inaccurate dates.

6.5 Evaluation of Methods

For future tephrostratigraphy studies in Arctic marine sediments, it may be appropriate to add additional steps during sample preparation in order to reduce the background noise observed in Fig. 8b (Appendix C; Fig. C1). The high minerogenic content in these samples resulted in elevated shard-count uncertainties, especially in the bottom of section 4. An HCl treatment, and additional centrifuge steps might have been good in order to prevent this background noise.

In this study, shards are reported per (ws) volume and (ws) weight, which may generate results with a different degree of accuracy. Although, it's more essential that shard concentrations within the same sample size are reported with the same units. As mentioned earlier, reporting shard concentrations per dry sediment weight would also have made the results easier to compare with previous studies.

7. Conclusion

It's unclear whether primary ash-fall deposit of either the Old Crow or Rauchua volcanic events reached the southern LR. The recorded 'background' tephra signal is most likely related to sea-ice or iceberg redeposition. The identified peak in tephra deposition may have been related to a single depositional event, potentially derived from secondary transport, where redeposition caused by bottom-currents and slope-mechanisms is considered likely. The heterogeneous morphologies observed throughout the studied sequence could be related to the incorporation of tephras from multiple volcanic events at the site, of a North Pacific arc origin.

The obtained tephra profile appears to have a better fit with Model 1 (Quartz-based OSL dating), mainly due to the fact that tephra shards were present near the core-bottom. Therefore a basal age of early MIS 5 is considered more likely. Additionally, the L2- and L1-segments appear to align with phases of increased sea-ice deposition. Neither the Old Crow or Rauchua horizons were identified in Model 2.

8. Acknowledgments

I would like to express a special thanks to my supervisor, Flor Vermassen, for assigning me this project, introducing me to paleoenvironmental research and for providing guidance throughout this project. Furthermore, I want to thank Simon Larsson for introducing me to tephrochronology, and for enabling this project by providing help and guidance during all laboratory and microscopy procedures. Lastly, I want to thank my family and friends for all their support during this process.

9. References

This report used the reference system *Cite Them Right 12th Edition – Harvard.*

Abbott, P.M. *et al.* (2018a) 'Tracing marine cryptotephras in the North Atlantic during the last glacial period: Protocols for identification, characterisation and evaluating depositional controls', *Marine Geology*, 401, pp. 81–97. Available at: https://doi.org/10.1016/j.margeo.2018.04.008.

Abbott, P.M. *et al.* (2018b) 'Tracing marine cryptotephras in the North Atlantic during the last glacial period: Protocols for identification, characterisation and evaluating depositional controls', *Marine Geology*, 401, pp. 81–97. Available at: https://doi.org/10.1016/j.margeo.2018.04.008.

Alatarvas, R., O'Regan, M. and Strand, K. (2022) 'Heavy mineral assemblages of the De Long Trough and southern Lomonosov Ridge glacigenic deposits: implications for the East Siberian Ice Sheet extent', *Climate of the Past*, 18(8), pp. 1867–1881. Available at: https://doi.org/10.5194/cp-18-1867-2022.

Bablon, M. *et al.* (2022) 'Holocene Marine Tephra Offshore Ecuador and Southern Colombia: First Trench-to-Arc Correlations and Implication for Magnitude of Major Eruptions', *Geochemistry, Geophysics, Geosystems*, 23(9), p. e2022GC010466. Available at: https://doi.org/10.1029/2022GC010466.

Bennett, K.D. *et al.* (1992) 'Holocene History of Environment, Vegetation and Human Settlement on Catta Ness, Lunnasting, Shetland', *Journal of Ecology*, 80(2), pp. 241–273. Available at: https://doi.org/10.2307/2261010.

Berger, A. and Loutre, M.F. (2010) 'Modeling the 100-kyr glacial–interglacial cycles', *Global and Planetary Change*, 72(4), pp. 275–281. Available at: https://doi.org/10.1016/j.gloplacha.2010.01.003.

Blockley, S.P.E. *et al.* (2005) 'A new and less destructive laboratory procedure for the physical separation of distal glass tephra shards from sediments', *Quaternary Science Reviews*, 24(16), pp. 1952–1960. Available at: https://doi.org/10.1016/j.quascirev.2004.12.008.

Bolin Centre for Climate Research (2014) *Cruise report - Leg 2 - Appendix SC - 3*. Appendix. Stockholm: Stockholm University. Available at: https://bolin.su.se/data/oden-swerus-2014-expedition-3.

Bolin Centre for Climate Research, S.U. (2024) *Data from expedition SWERUS-C3, Arctic Ocean, 2014 | Bolin Centre Database*. Available at: https://doi.org/10.17043/oden-swerus-2014-expedition-3.

Brendryen, J., Haflidason, H. and Sejrup, H.P. (2010) 'Norwegian Sea tephrostratigraphy of marine isotope stages 4 and 5: Prospects and problems for tephrochronology in the North Atlantic region', *Quaternary Science Reviews*, 29(7), pp. 847–864. Available at: https://doi.org/10.1016/j.quascirev.2009.12.004.

Bubenshchikova, N. *et al.* (2024) 'The Pauzhetka tephra (South Kamchatka): A key middle Pleistocene isochron for the Northwest Pacific and Okhotsk Sea sediments', *Quaternary Geochronology*, 79, p. 101476. Available at: https://doi.org/10.1016/j.quageo.2023.101476.

Carlson, T.B. (2018) *Volcanic Glass as a Paleoenvironmental Proxy: Comparing Preparation Methods on Ashes from the Comparing Preparation Methods on Ashes from the Lee of the Cascade Range in Oregon, USA Lee of the Cascade Range in Oregon, USA*. Master Thesis. Oregon, USA: Portland State University.

Cashman, K.V. and Rust, A.C. (2020) 'Far-travelled ash in past and future eruptions: combining tephrochronology with volcanic studies', *Journal of Quaternary Science*, 35(1–2), pp. 11–22. Available at: https://doi.org/10.1002/jqs.3159.

Colleoni, F. *et al.* (2016) 'Constraint on the penultimate glacial maximum Northern Hemisphere ice topography (≈140 kyrs BP)', *Quaternary Science Reviews*, 137, pp. 97–112. Available at: https://doi.org/10.1016/j.quascirev.2016.01.024.

Darby, D.A., Bischof, J.F. and Jones, G.A. (1997) 'Radiocarbon chronology of depositional regimes in the western Arctic Ocean', *Deep Sea Research Part II: Topical Studies in Oceanography*, 44(8), pp. 1745–1757. Available at: https://doi.org/10.1016/S0967-0645(97)00039-8.

Davies, L.J. *et al.* (2016) 'Late Pleistocene and Holocene tephrostratigraphy of interior Alaska and Yukon: Key beds and chronologies over the past 30,000 years', *Quaternary Science Reviews*, 146, pp. 28–53. Available at: https://doi.org/10.1016/j.quascirev.2016.05.026.

Davies, S.M. *et al.* (2005) 'Detection of Lateglacial distal tephra layers in the Netherlands', *Boreas*, 34(2), pp. 123–135. Available at: https://doi.org/10.1111/j.1502-3885.2005.tb01010.x.

Davies, S.M. (2015) 'Cryptotephras: the revolution in correlation and precision dating', *Journal of Quaternary Science*, 30(2), pp. 114–130. Available at: https://doi.org/10.1002/jqs.2766.

Derkachev, A. *et al.* (2023) 'Tephrostratigraphy of Pleistocene-Holocene deposits from the Detroit Rise eastern slope (northwestern Pacific)', *Frontiers in Earth Science*, 10. Available at: https://doi.org/10.3389/feart.2022.971404.

Derkachev, A.N. *et al.* (2020) 'Middle to late Pleistocene record of explosive volcanic eruptions in marine sediments offshore Kamchatka (Meiji Rise, NW Pacific)', *Journal of Quaternary Science*, 35(1–2), pp. 362–379. Available at: https://doi.org/10.1002/jqs.3175.

Dugmore, A. (1989) 'Icelandic Volcanic Ash in Scotland', *SCOTTISH GEOGRAPHICAL MAGAZINE*, 105(3), pp. 168–172. Available at: https://doi.org/10.1080/14702548908554430.

Dypvik, H. and Harris, N.B. (2001) 'Geochemical facies analysis of fine-grained siliciclastics using Th/U, Zr/Rb and (Zr+Rb)/Sr ratios', *Chemical Geology*, 181(1), pp. 131–146. Available at: https://doi.org/10.1016/S0009-2541(01)00278-9.

Eldevik, T. and Nilsen, J.E.Ø. (2013) 'The Arctic–Atlantic Thermohaline Circulation', *Journal of Climate*, 26(21), pp. 8698–8705. Available at: https://doi.org/10.1175/JCLI-D-13-00305.1.

Elias, S.A. (2023) 'Introduction', in *Reference Module in Earth Systems and Environmental Sciences*. Elsevier. Available at: https://doi.org/10.1016/B978-0-323-99931-1.00095-7.

Enache, M.D. and Cumming, B.F. (2006) 'The Morphological and Optical Properties of Volcanic Glass: A Tool to Assess Density-induced Vertical Migration of Tephra in Sediment Cores', *Journal of Paleolimnology*, 35(3), pp. 661–667. Available at: https://doi.org/10.1007/s10933-005-3604-9.

Freundt, A. *et al.* (2023) 'Tephra layers in the marine environment: a review of properties and emplacement processes', in *Volcanic Processes in the Sedimentary Record: When Volcanoes Meet the Environment*. United Kingdom of Great Britain and Northern Ireland: Geological Society of London.

Gehrels, M.J. *et al.* (2006) 'A continuous 5300-yr Holocene cryptotephrostratigraphic record from northern New Zealand and implications for tephrochronology and volcanic hazard assessment', *The Holocene*, 16(2), pp. 173–187. Available at: https://doi.org/10.1191/0959683606hl918rp.

Graham, R.W. *et al.* (2016) 'Timing and causes of mid-Holocene mammoth extinction on St. Paul Island, Alaska', *Proceedings of the National Academy of Sciences*, 113(33), pp. 9310–9314. Available at: https://doi.org/10.1073/pnas.1604903113.

Griggs, A.J. *et al.* (2014) 'Optimising the use of marine tephrochronology in the North Atlantic: a detailed investigation of the Faroe Marine Ash Zones II, III and IV', *Quaternary Science Reviews*, 106, pp. 122–139. Available at: https://doi.org/10.1016/j.quascirev.2014.04.031.

Hällgren, J. (2015) *Arctic Ocean glacial/interglacial regimes over the Late Quaternary*. Bachelor Thesis. Stockholm: Stockholms Univerity.

Jakobsson, M. *et al.* (2000) 'Manganese and color cycles in Arctic Ocean sediments constrain Pleistocene chronology', *Geology*, 28(1), pp. 23–26. Available at: https://doi.org/10.1130/0091-7613(2000)28<23:MACCIA>2.0.CO;2.

Jakobsson, M. *et al.* (2003) 'Optically Stimulated Luminescence dating supports central Arctic Ocean cm-scale sedimentation rates', *Geochemistry, Geophysics, Geosystems*, 4(2). Available at:https://doi.org/10.1029/2002GC000423.

Jakobsson, M. *et al.* (2016) 'Evidence for an ice shelf covering the central Arctic Ocean during the penultimate glaciation', *Nature Communications*, 7(1), p. 10365. Available at: https://doi.org/10.1038/ncomms10365.

Jokat, W. *et al.* (1992) 'Lomonosov Ridge—A double-sided continental margin', *Geology*, 20(10), pp. 887–890. Available at: https://doi.org/10.1130/0091-7613(1992)020<0887:LRADSC>2.3.CO;2.

Katoh, S. *et al.* (2000) 'Chronostratigraphy and correlation of the Plio-Pleistocene tephra layers of the Konso Formation, southern Main Ethiopian Rift, Ethiopia', *Quaternary Science Reviews*, 19(13), pp. 1305–1317. Available at: https://doi.org/10.1016/S0277-3791(99)00099-2.

Khare, N. and Khare, R. (2021) 'Chapter 9 - Arctic Ocean circulation', in N. Khare and R. Khare (eds) *The Arctic*. Elsevier, pp. 127–137. Available at: https://doi.org/10.1016/B978-0-12-823735-9.00006-0.

Kotov, A.N. (1998) *Alasny i ledovy komplexy otlozhenii Severo-zapadnoi Chukotki (Alas and ice complexes of the northwestern Chukotka deposits) [in Russian], Cryosphera Zemli, II(1), 11–18.*

Kyle, P.R., Ponomareva, V.V. and Rourke Schluep, R. (2011) 'Geochemical characterization of marker tephra layers from major Holocene eruptions, Kamchatka Peninsula, Russia', *International Geology Review*, 53(9), pp. 1059–1097. Available at: https://doi.org/10.1080/00206810903442162.

Larsson, S.A. (2022) 'Ashes to ashes : Applications of tephrochronology in Scandinavia'. Available at: https://urn.kb.se/resolve?urn=urn:nbn:se:su:diva-199504 (Accessed: 22 May 2024).

Lisiecki, L.E. and Raymo, M.E. (2005) 'A Pliocene-Pleistocene stack of 57 globally distributed benthic δ18O records', *Paleoceanography*, 20(1). Available at: https://doi.org/10.1029/2004PA001071.

Lowe, D.J. (2011) 'Tephrochronology and its application: A review', *Quaternary Geochronology*, 6(2), pp. 107–153. Available at: https://doi.org/10.1016/j.quageo.2010.08.003.

Lowe, D.J. *et al.* (2017) 'Correlating tephras and cryptotephras using glass compositional analyses and numerical and statistical methods: Review and evaluation', *Quaternary Science Reviews*, 175, pp. 1–44. Available at: https://doi.org/10.1016/j.quascirev.2017.08.003.

Lowe, D.J. and Hunt, J.B. (2001) *A summary of terminology used in tephra-related studies*. Journal Article. Waikato: The University of Waikato. Available at: https://hdl.handle.net/10289/3526.

Lu, Z. and Dzurisin, D. (2014) 'Tectonic Setting of Aleutian Volcanism', in Z. Lu and D. Dzurisin (eds) *InSAR Imaging of Aleutian Volcanoes: Monitoring a Volcanic Arc from Space*. Berlin, Heidelberg: Springer, pp. 49–69. Available at: https://doi.org/10.1007/978-3-642-00348-6_4.

McLean, D. *et al.* (2018) 'Integrating the Holocene tephrostratigraphy for East Asia using a high-resolution cryptotephra study from Lake Suigetsu (SG14 core), central Japan', *Quaternary Science Reviews*, 183, pp. 36–58. Available at: https://doi.org/10.1016/j.quascirev.2017.12.013.

Miller, T.P., Waythomas, C.F. and Gardner, J.E. (2002) 'Possible Multiple Late Quaternary Caldera-Forming Eruptions at Mount Veniaminof Volcano, Alaska Peninsula', 2002, pp. V11A-1376.

Nowaczyk, N.R. *et al.* (2013) 'Chronology of Lake El'gygytgyn sediments – a combined magnetostratigraphic, palaeoclimatic and orbital tuning study based on multi-parameter analyses', *Climate of the Past*, 9(6), pp. 2413–2432. Available at: https://doi.org/10.5194/cp-9-2413-2013.

O'Regan, M. *et al.* (2020) 'Calcareous nannofossils anchor chronologies for Arctic Ocean sediments back to 500 ka', *Geology*, 48(11), pp. 1115–1119. Available at: https://doi.org/10.1130/G47479.1.

Otvos, E.G. (2015) 'The Last Interglacial Stage: Definitions and marine highstand, North America and Eurasia', *Quaternary International*, 383, pp. 158–173. Available at: https://doi.org/10.1016/j.quaint.2014.05.010.

Pearce, C. *et al.* (2017) 'The 3.6 ka Aniakchak tephra in the Arctic Ocean: a constraint on the Holocene radiocarbon reservoir age in the Chukchi Sea', *Climate of the Past*, 13(4), pp. 303–316. Available at: https://doi.org/10.5194/cp-13-303-2017.

Pearce, N.J.G. *et al.* (2004) 'Identification of Aniakchak (Alaska) tephra in Greenland ice core challenges the 1645 BC date for Minoan eruption of Santorini', *Geochemistry, Geophysics, Geosystems*, 5(3). Available at: https://doi.org/10.1029/2003GC000672.

Platz, T. *et al.* (2007) 'Improving the reliability of microprobe-based analyses of andesitic glasses for tephra correlation', *The Holocene*, 17(5), pp. 573–583. Available at: https://doi.org/10.1177/0959683607078982.

Ponomareva, V. *et al.* (2013) 'Identification of a widespread Kamchatkan tephra: A middle Pleistocene tie-point between Arctic and Pacific paleoclimatic records', *Geophysical Research Letters*, 40(14), pp. 3538–3543. Available at: https://doi.org/10.1002/grl.50645.

Ponomareva, V. *et al.* (2015) 'Tephra from andesitic Shiveluch volcano, Kamchatka, NW Pacific: chronology of explosive eruptions and geochemical fingerprinting of volcanic glass', *International Journal of Earth Sciences*, 104(5), pp. 1459–1482. Available at: https://doi.org/10.1007/s00531-015-1156-4.

Ponomareva, V. *et al.* (2018) 'Holocene tephra from the Chukchi-Alaskan margin, Arctic Ocean: Implications for sediment chronostratigraphy and volcanic history', *Quaternary Geochronology*, 45, pp. 85–97. Available at: https://doi.org/10.1016/j.quageo.2017.11.001.

Ponomareva, V.V. *et al.* (2004) 'The 7600 (14C) year BP Kurile Lake caldera-forming eruption, Kamchatka, Russia: stratigraphy and field relationships', *Journal of Volcanology and Geothermal Research*, 136(3), pp. 199–222. Available at: https://doi.org/10.1016/j.jvolgeores.2004.05.013.

Ponomareva, V.V. *et al.* (2023) 'A 6.2 Ma-Long Record of Major Explosive Eruptions From the NW Pacific Volcanic Arcs Based on the Offshore Tephra Sequences on the Northern Tip of the Emperor Seamount Chain', *Geochemistry, Geophysics, Geosystems*, 24(12), p. e2023GC011126. Available at: https://doi.org/10.1029/2023GC011126.

Preece, S.J. *et al.* (2011) 'Old Crow tephra across eastern Beringia: a single cataclysmic eruption at the close of Marine Isotope Stage 6', *Quaternary Science Reviews*, 30(17), pp. 2069–2090. Available at: https://doi.org/10.1016/j.quascirev.2010.04.020.

Railsback, L.B. *et al.* (2015) 'An optimized scheme of lettered marine isotope substages for the last 1.0 million years, and the climatostratigraphic nature of isotope stages and substages', *Quaternary Science Reviews*, 111, pp. 94–106. Available at: https://doi.org/10.1016/j.quascirev.2015.01.012.

Reyes, A.V. *et al.* (2022) 'Detrital glass in a Bering Sea sediment core yields a ca. 160 ka Marine Isotope Stage 6 age for Old Crow tephra', *Geology*, 51(1), pp. 106–110. Available at: https://doi.org/10.1130/G50491.1.

Schindlbeck-Belo, J.C. *et al.* (2024) 'PalVol v1: a proxy-based semi-stochastic ensemble reconstruction of volcanic stratospheric sulfur injection for the last glacial cycle (140 000–50 BP)', *Earth System Science*

Data, 16(2), pp. 1063–1081. Available at: https://doi.org/10.5194/essd-16-1063-2024.

Shu, Q. *et al.* (2022) 'Arctic Ocean Amplification in a warming climate in CMIP6 models', *Science Advances*, 8(30), p. eabn9755. Available at: https://doi.org/10.1126/sciadv.abn9755.

Strunk, A. *et al.* (2020) 'Improving the reliability of bulk sediment radiocarbon dating', *Quaternary Science Reviews*, 242, p. 106442. Available at: https://doi.org/10.1016/j.quascirev.2020.106442.

Thordarson, T. and Self, S. (2003) 'Atmospheric and environmental effects of the 1783–1784 Laki eruption: A review and reassessment', *Journal of Geophysical Research: Atmospheres*, 108(D1), p. AAC 7-1-AAC 7-29. Available at: https://doi.org/10.1029/2001JD002042.

Timmermans, M.-L. and Toole, J.M. (2023) 'The Arctic Ocean's Beaufort Gyre', *Annual Review of Marine Science*, 15(Volume 15, 2023), pp. 223–248. Available at: https://doi.org/10.1146/annurev-marine-032122-012034.

Turney, C.S.M. (1998) 'Extraction of rhyolitic component of Vedde microtephra from minerogenic lake sediments', *JOURNAL OF PALEOLIMNOLOGY*, 19(2), pp. 199–206. Available at: https://doi.org/10.1023/A:1007926322026.

Vanderaveroet, P. *et al.* (1999) 'A record of glacial/interglacial alternations in Pleistocene sediments off New Jersey expressed by clay mineral, grain-size and magnetic susceptibility data', *Marine Geology*, 159(1), pp. 79–92. Available at: https://doi.org/10.1016/S0025-3227(98)00203-5.

West, G. *et al.* (2021) 'Optically stimulated luminescence dating supports pre-Eemian age for glacial ice on the Lomonosov Ridge off the East Siberian continental shelf', *Quaternary Science Reviews*, 267, p. 107082. Available at: https://doi.org/10.1016/j.quascirev.2021.107082.

Westgate, J.A., Hamilton, T.D. and Gorton, M.P. (1983) 'Old Crow tephra: A new late Pleistocene stratigraphic marker across north-central Alaska and western Yukon Territory', *Quaternary Research*, 19(1), pp. 38–54. Available at: https://doi.org/10.1016/0033-5894(83)90026-1.

10. Appendix

10.1 Appendix A

Table A1
Locations of all marine cores mentioned in the text.

Core	Coordinates	Location
SWERUS-L2-29-GC1	81.299356°N 141.78255°E	Southern Lomonosov Ridge
HLY0501-1	72.906000°N 158.422000°W	Chukchi shelf, NE Alaska
SWERUS-L2-29-PC1	72.516580°N 175.319605°W	Chukchi Sea
U1345	60.150000°N 179.500000°W	Bering Sea
SO201-2-40 KL	53.310500°N 164.777800°E	Bering Sea
SO201-2-81 KL	56.716500°N 170.496200°E	NW Pacific Ocean

PS2757-8	81.1633°N 140.2°E	Southern Lomonosov Ridge
ICDP 5011-1	67.495210°N 172.052809°E	Lake El'gygytgyn
96/12-1pc	87.098333°N 144.773333°E	Central LR ridge
SWERUS-L2-32-GC2	85.152613°N 151.664309°E	Central LR ridge

10.2 Appendix B

Table B1
Core depth-interval with corresponding LAB ID for low-resolution samples.

Core depth (mbsf)	LAB ID
1.06 - 1.16	Sec. 2: 90-100
1.16 - 1.26	Sec. 2: 100-110
1.26 - 1.36	Sec. 2: 110-120
1.36 - 1.46	Sec. 2: 120-130
1.46 - 1.56	Sec. 2: 130-140
1.56 - 1.66	Sec. 2: 140-150
1.66 - 1.76	Sec. 3: 0-10
1.76 - 1.86	Sec. 3: 10-20
1.86 - 1.96	Sec. 3: 20-30
1.96 - 2.06	Sec. 3: 30-40
2.06 - 2.16	Sec. 3: 40-50
2.16 - 2.26	Sec. 3: 50-60
2.26 - 2.36	Sec. 3: 60-70
2.36 - 2.46	Sec. 3: 70-80
2.46 - 2.56	Sec. 3: 80-90
2.56 - 2.66	Sec. 3: 90-100
2.66 - 2.76	Sec. 3: 100-110
2.76 - 2.86	Sec. 3: 110-120
2.86 - 2.96	Sec. 3: 120-130
2.96 - 3.06	Sec. 3: 130-140
3.06 - 3.16	Sec. 3: 140-150
3.16 - 3.26	Sec. 4: 0-10
3.26 - 3.36	Sec. 4: 10-20
3.36 - 3.46	Sec. 4: 20-30
3.46 - 3.56	Sec. 4: 30-40
3.56 - 3.66	Sec. 4: 40-50
3.66 - 3.76	Sec. 4: 50-60
3.76 - 3.86	Sec. 4: 60-70
3.86 - 3.96	Sec. 4: 70-80
3.96 - 4.06	Sec. 4: 80-90

Table B2
Core depth-interval with corresponding LAB ID for low-resolution samples.

Core depth (mbsf)	LAB ID
2.35 - 2.36	Sec. 3: 69-70
2.36 - 2.37	Sec. 3: 70-71
2.37 - 2.38	Sec. 3: 71-72
2.38 - 2.39	Sec. 3: 72-73
2.39 - 2.40	Sec. 3: 73-74
2.40 - 2.41	Sec. 3: 74-75
2.41 - 2.42	Sec. 3: 75-76
2.42 - 2.43	Sec. 3: 76-77
2.43 - 2.44	Sec. 3: 77-78
2.44 - 2.45	Sec. 3: 78-79
2.45 - 2.46	Sec. 3: 79-80
2.46 - 2.47	Sec. 3: 80-81

4.06 - 4.16	Sec. 4: 90-100
4.16 - 4.26	Sec. 4: 100-110
4.26 - 4.36	Sec. 4: 110-120
4.36 - 4.46	Sec. 4: 120-130
4.46 - 4.56	Sec. 4: 130-140
4.56 - 4.66	Sec. 4: 140-150

10.3 Appendix C

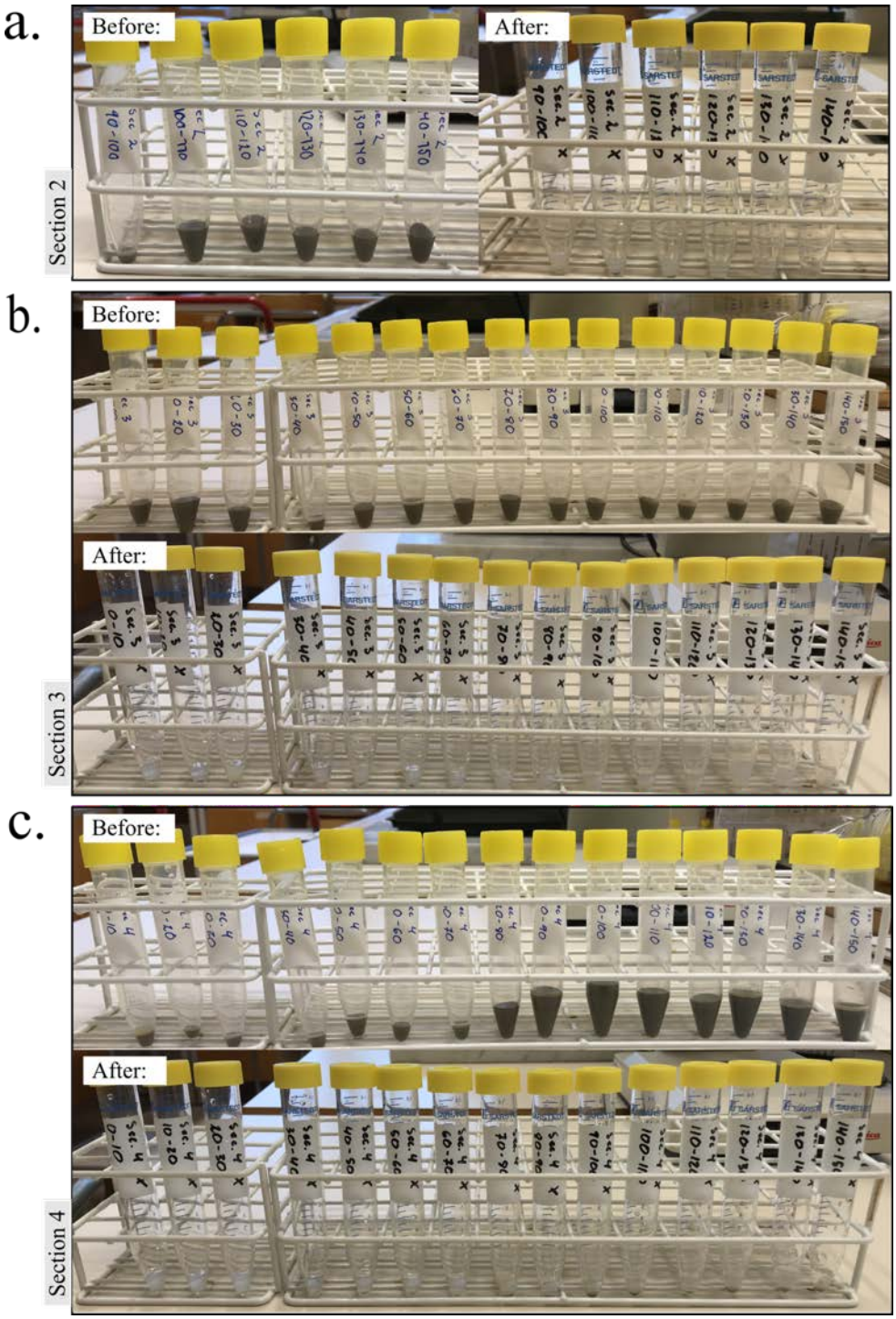

Fig. C1. Before Photos of the original low-resolution samples before density separation, centrifuging and extraction. After Photos show the final extracted material i.e the 'tephra sample'. **a)** Section 2: 90-150 cm (6 samples) Before and After. **b)** Section 3: 0-150 cm (15 samples) Before and After. **c)** Section 4: 0-150 cm (15 samples) Before and After. A high content of minerogenic content was observed in the bottom.

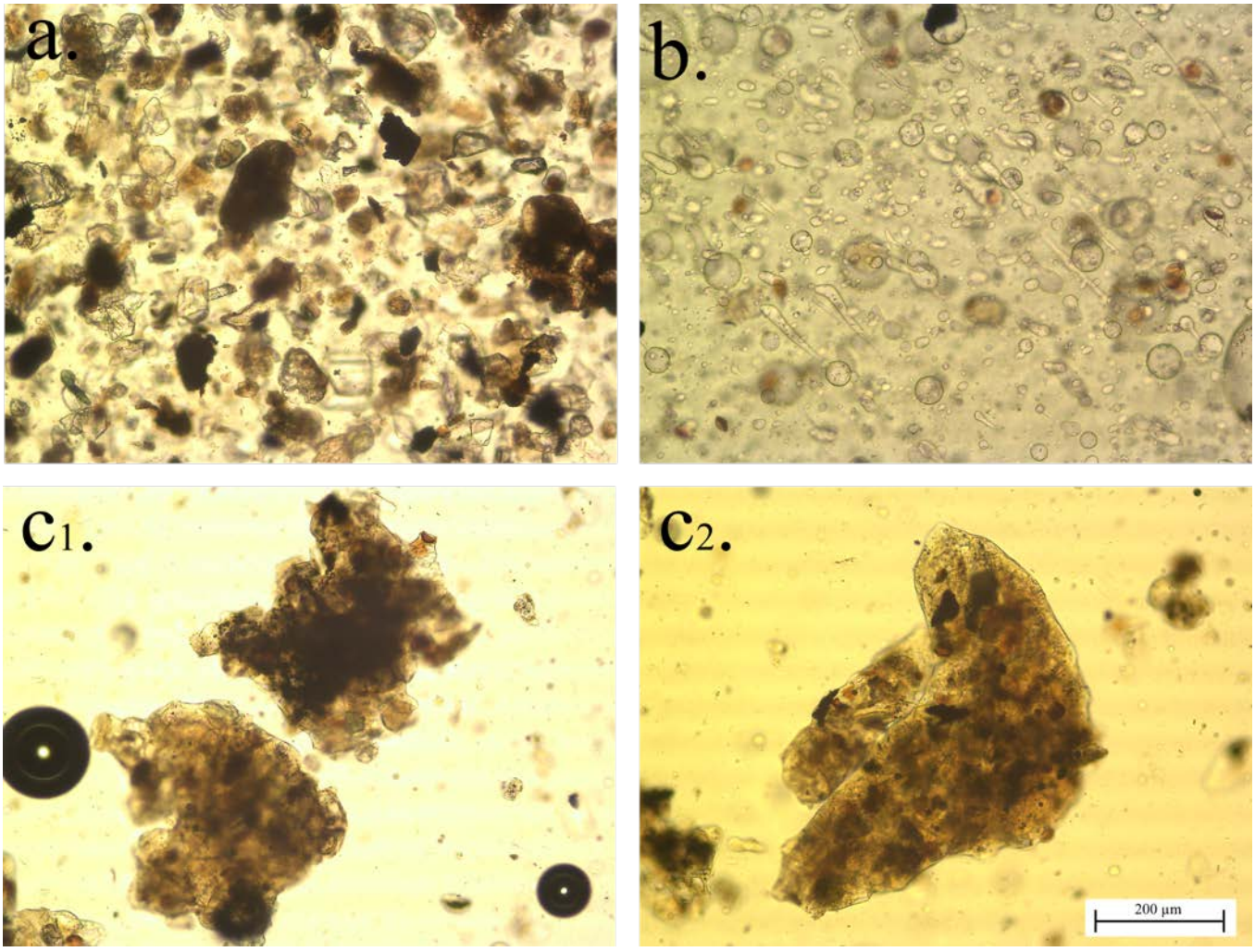

Fig. C2. Pictures of background noise recorded in a few samples. **a.)** High-minerogenic content observed in the low-ermost samples of section 4 (low-resolution samples**). b)** Layers of air bubbles in a high-resolution sample. **c_1)** and **c_2)** Aggregated material in a high-resolution sample.